1 **Integrating field, textural and geochemical monitoring to track eruption triggers and**

2 **dynamics: a case-study from Piton de la Fournaise**

4 Lucia Gurioli[1], Andrea Di Muro[2], Ivan Vlastélic[1], Séverine Moune[1], Simon Thivet[1],

5 Marina Valer[1], Nicolas Villeneuve[2], Guillaume Boudoire[2,3], Aline Peltier[2], Patrick

6 Bachèlery[1], Valerie Ferrazzini[2], Nicole Métrich[2], Mhammed Benbakkar[1], Nicolas

7 Cluzel[1], Christophe Constantin[1], Jean-Luc Devidal[1], Claire Fonquernie[1], Jean-Marc

8 Hénot[1]

9 (1) Université Clermont Auvergne, CNRS, IRD, OPGC, Laboratoire Magmas et Volcans, F-63000

10 Clermont-Ferrand, France

11 (2) Institut de Physique du Globe (IPGP), Sorbonne Paris-Cite, CNRS UMR-7154, Université Paris

12 Diderot, Observatoire Volcanologique du Piton de la Fournaise (OVPF), Bourg Murat, France,

13 (3) Laboratoire Géosciences Réunion, Université de La Réunion, Institut de Physique du Globe de

14 Paris, Sorbonne Paris-Cité, UMR 7154 CNRS, F-97715 Saint-Denis, France

15 Corresponding author: L Gurioli, Université Clermont Auvergne, CNRS, IRD, OPGC, LMV

16 Campus Universitaire des Cézeaux, 6 Avenue Blaise Pascal, 63178 Aubière Cedex

17 (lucia.gurioli@uca.fr)

19 **Abstract**

20 The 2014 eruption at Piton de la Fournaise (PdF), La Réunion, which occurred after 41

21 months of quiescence, began with surprisingly little precursory activity, and was one of the

22 smallest so far observed at PdF in terms of duration (less than 2 days) and volume (less than

23 0.4×10^6 m^3). The pyroclastic material was composed of spiny-opaque, spiny-iridescent, and

24 fluidal basaltic scoria along with golden basaltic pumice. Density analyses performed on 200

25 lapilli reveal that the spiny-opaque clasts are the densest (1600 kg/m^3) and richest in crystals

26 (55 vol%), and the golden pumices are the lightest (400 kg/m^3) and poorest in crystals (8

27 vol%). The connectivity data indicate that the fluidal and golden (Hawaiian-like) clasts have

28 more isolated vesicles (up to 40%) than the spiny (Strombolian-like) clasts (0-5%). These

29 textural variations are linked to primary pre-eruptive magma storage conditions. The golden

30 and fluidal fragments track the hotter portion of the melt, in contrast to the spiny fragments

31 and lava that mirror the cooler portion of the shallow reservoir. Exponential decrease of the

32 magma ascent and output rates corresponded to progressive tapping of these distinct portions

of the storage system. Increasing syn-eruptive degassing and melt-gas decoupling lead to a decrease in the explosive intensity from early fountaining to Strombolian activity. The geochemical results confirm the absence of new hot input of magma into the 2014 reservoir and confirm the emission of a single, shallow, differentiated magma source, possibly related to residual magma from the November 2009 eruption. Fast volatile exsolution and crystal-melt separation (second boiling) were triggered by deep pre-eruptive magma transfer and stress field change. Our study highlights the possibility that shallow magma pockets can be quickly reactivated by deep processes without mass or energy (heat) transfer and produce hazardous eruptions with only short term elusive precursors.

Key words : Piton de la Fournaise, Hawaiian activity, Strombolian activity, shallow reservoire, texture, petrology, geochemistry

1. Introduction

A detailed characterization and understanding of eruptive dynamics and of processes driving and modulating volcano unrest is crucial in monitoring active volcanoes and fundamental for forecasting volcanic eruptions (Sparks, 2003). Many studies suggest that eruptive phenomena are strongly dependent on the physico-chemical properties of ascending magma in the conduit (e.g., temperature, viscosity, porosity, and permeability) (e.g. Sparks, 1978; Rust and Cashman, 2011; Gonnermann and Manga, 2013; Polacci et al., 2014). Integrating petrographic, chemical and textural data can thus provide critical information to constrain both the pre-eruptive storage conditions, and the processes related to magma ascent, degassing and cooling (e.g., reference in Table 1 in Gurioli et al., 2015). This multidisciplinary approach is of even greater importance in the monitoring of volcanoes which emit relatively uniform magma compositions over time, like basaltic volcanoes (e.g. Di Muro et al., 2014; Gurioli et al., 2015; Coppola et al., 2017). As a result, monitoring of textures, and petrochemical properties of lava fragments and pyroclasts is now routinely carried out on a daily basis at active volcanoes such as Kilauea, Etna, and Stromboli (e.g., Thornber et al., 2003; Polacci et al., 2006; Swanson et al., 2009; Taddeucci et al., 2002; Colo' et al., 2010; Houghton et al., 2011; 2013; 2016; Carey et al., 2012; 2013; Lautze et al., 2012; Andronico et al., 2013a; b; 2014; Corsaro and and Miraglia, 2014; Di Muro et al., 2014; Eychenne et al., 2015; Gurioli et al.; 2014; Leduc et al., 2015; Kahl et al., 2015). In the past, time series of petrographic and geochemical data have been measured for Piton de la Fournaise (PdF) basalts and particularly for effusive products. The aim of these datasets was

65 to constrain time and space magma evolution for one of the most active basaltic volcanoes of

66 the world (e.g. Albarède et al., 1997; Vlastélic et al., 2005; 2007, 2009; Vlastèlic and

67 Pietruszka, 2016; Schiano et al., 2012; Boivin and Bachèlery, 2009; Peltier et al., 2009; Lénat

68 et al., 2012; Di Muro et al., 2014; 2015). However, this type of approach has seldom been

69 coupled with detailed textural studies at PdF and instead has mostly focused on crystal

70 textures and crystal size distribution (Welsch et al., 2009; 2013; Di Muro et al., 2014; 2015).

71 Moreover, only sporadic data exist on the textures of pyroclasts ejected by the PdF (Villemant

72 et al., 2009; Famin et al., 2009; Michon et al., 2013; Vlastélic et al., 2013; Welsch et al., 2009;

73 2013; Morandi et al., 2016; Di Muro et al., 2015; Ort et al., 2016).

74   Within this paper, we present a multidisciplinary textural, chemical and petrological

75 approach to quantify and understand the short-lived 2014 PdF eruption. This approach

76 combines detailed study of the pyroclastic deposit (grain size and componentry) with bulk

77 texture analysis (density, vesicularity, connectivity, permeability, morphology, vesicle

78 distribution and crystal content) and a petro-chemical study (bulk rock, glass, minerals, melt

79 inclusions) of the same clasts. This integrated approach has now been formalized within the

80 French National Observation Service for Volcanology (SNOV), as routine observational

81 systems   (DynVolc),   Dynamics   of   Volcanoes,   (http://wwwobs.univ-

82 bpclermont.fr/SO/televolc/dynvolc/) and GazVolc, Observation des gaz volcaniques,

83 (http://wwwobs.univ-bpclermont.fr/SO/televolc/gazvolc) to provide data for the on-going

84 activity at PdF (Harris et al., 2017).

85   In spite of being the first of a series of eruptions, the June 2014 event was preceded by

86 only weak inflation and by a rapid increase in number of shallow (< 2 km below volcano

87 summit) volcano tectonic earthquakes that happened only 11 days before the eruption (Peltier

88 et al., 2016). The eruptive event was dominantly effusive, lasted only 20 hours and emitted a

89 very small volume of magma (ca. 0.4×10^6 m^3, Peltier et al., 2016), which makes this event

90 one of the smallest, in terms of duration and volume, observed at PdF up to now. In addition,

91 the eruption started during the night and very little direct observation exists for the first few

92 hours of the activity, when the lava effusion was associated with very weak fountaining

93 activity and Strombolian explosions.

94   This eruption occurred just outside the southern border of the summit Dolomieu

95 caldera, at the top of the central cone of PdF (Fig. 1). This is a high risk sector because of the

96 high number of tourists. Identification of precursors of this kind of activity represents an

97 important challenge for monitoring systems (Bachélery et al., 2016).

98   Therefore this eruption represents an ideal context to apply our multidisciplinary

99 approach, with the aim of addressing the following key questions:

100   (i)   why was such a small volume of magma erupted instead of remaining
101   intruded?

102   (ii)   what caused the rapid trigger and the sudden end to this small volume
103   eruption?

104   (iii)   which was the source of the eruption (shallow versus deep, single versus
105   multiple small magma batches)?

106   (iv)   what was the ascent and degassing history of the magma?

107   (v)   what was the time and space evolution of the eruptive event?

108 Furthermore, this eruption provides an exceptional opportunity to study processes leading to
109 the transition from mild Hawaiian (<20 m high fountains, following the nomenclature
110 proposed by Stovall et al., 2011) to Strombolian activity (<10 m high explosions), whose
111 products are little modified by post-fragmentation processes because of the very low intensity
112 of the activity.

113 **2 The 2014 activity**

114 **2.1 Precursory activity**

115 The 20 June 2014 summit eruption represents the first eruption at PdF after 41 months of
116 quiescence. The last eruption had been on 9 December 2010, with a shallow (above sea level)
117 intrusion on 2 February 2011 (Roult et al., 2012). From 2011, the deformation at PdF was
118 constant with two distinct types of behaviour: (i) a summit contraction of a few centimetres
119 every year (Fig. 1d); (ii) a preferential displacement of the east flank at a rate of 1-3
120 centimetres per year (Brenguier et al., 2012; Staudacher and Peltier, 2015). The background
121 microseismicity was very low (< 5 shallow events/day below volcano summit) and low-
122 temperature summit intracaldera fumaroles emitted very little sulphur (H_2S or SO_2) and
123 carbon (CO_2) (Di Muro et al., 2016). After 41 months of rest, a new intense cycle of activity
124 (June 2014, February 2015, May 2015, July 2015, August-October 2015; May 2016;
125 September 2016; January 2017 and July 2017) began with surprisingly little and ambiguous
126 precursory activity.

127   The 2014 summit eruption started during the night of June 20/21, at 21h35 GMT
128 (0h35 local time) and ended on June 21 at 17h09 GMT (21h09 local time), after less than 20
129 hours of dominantly effusive activity. The volcano reawakening was preceded, in March and
130 April 2014, by deep (15-20 km below sea level) eccentric seismicity and increase in soil CO_2

131   flux below the western volcano flank, 15 km NW of the volcano summit (Liuzzo et al., 2015;

132   Boudoire et al., 2017). Background micro-seismicity and inflation of the central cone

133   increased progressively starting on 9 June 2014. Weak inflation recorded on both distal and

134   summit baselines (Fig. 1d) suggest that deep (below sea level) magma up-rise was

135   pressurizing the shallow (above sea level) magma storage system (Peltier et al., 2016). On

136   June 13, 17 and 20, three shallow (hypocentres located above sea level) intense seismic crises

137   occurred below the summit Dolomieu caldera (Fig. 1), with hundreds of events located in a

138   narrow depth range between 1100 and 2100 metres below the volcano summit. These seismic

139   crises consisted of swarms of low magnitude (M: 1-2) volcano tectonic events which

140   increased in number from the first to the third crisis. On June 20, seismicity increased

141   progressively and a final seismic crisis started at 20h20 GMT, only 75 minutes before the

142   eruption. This last seismic crisis was coupled with acceleration in the deformation of the

143   summit area, which began only 60 minutes before the eruption. Interestingly, only slight

144   inflation of the central cone (< 2 cm of dilatation) was detected 11 days before the 2014

145   eruption with a maximum of 1 cm and 1.6 cm enlargement at the summit and the base of the

146   cone, respectively (Peltier et al., 2016 and Fig. 1d). A moderate increase in CO_2 and H_2S

147   emissions from summit intracaldera fumaroles was detected starting on June 2, but only very

148   minor SO_2 emissions occurred before the eruption (mostly on June 7 and 15, unpublished

149   data). Therefore, the acceleration in both geophysical and geochemical parameters was mostly

150   related to the late phase of dyke propagation towards the surface just before the eruption.

151   Following the end of the June 20-21 eruption, a long-term continuous inflation of the edifice

152   began, at a moderate rate, and mostly at the base of the volcano. More than one year after this

153   first eruption, the long-term deformation trends showed that the 2014 eruption marked a kink

154   between the deflation trend which followed the caldera-forming 2007 eruption (Staudacher et

155   al., 2009) and the currently ongoing continuous inflation trend (Fig. 1d, and Peltier et al.,

156   2016; Coppola et al., 2017).

2.2 Chronology of the events

158   We reconstructed the chronology of events by combining a distribution map of the fissures,

159   pyroclastic deposits and lava flows (Fig. 1) with a review of available images (visible and IR)

160   and videos extracted from the observatory data base, the local newspapers, and web sites (Fig.

161   2). The 2014 eruption occurred at the summit and on the SE slopes of the Dolomieu Caldera

162   (Figs. 1a, 1b and 1c) and evolved quickly and continuously over 20 hours. The full set of

163   fractures opened during a short period of time (minutes) and emitted short (<1.7 km long)

164 lava flows (Fig. 1 and Figs. 2c and 2d). Feeding vents were scattered along a 0.6 km long

165 fissure set (Fig. 1a) and produced very weak (low) Hawaiian to Strombolian activity (Fig. 2).

166   Fissures opened from west to east, initially sub-parallel to the southern border of

167 Dolomieu caldera and then propagated at lower altitude (Fig. 1). The summit part of the

168 fractures (ca. 2500 m asl, Western Fracture, WF in Fig. 1) emitted only small volumes of lava

169 and pyroclasts. This part of the fracture set was active only during the first few hours of the

170 eruption, at night. The eastern part of the fractures (Upper Fracture, UF in Fig. 1) descended

171 to lower altitude (between 2400 and 2300 m asl, Middle Fracture, Fig. 1) along the SE flank

172 of the summit cone and emitted most of the erupted volume. As often observed in PdF

173 eruptions, the activity progressively focused on a narrow portion of the fractures at low

174 altitude and finally on a single vent located at the lower tip of the fracture system (Main Vent,

175 at 2336 m asl, MV in Figs. 1, 2). The first in situ observations in the morning of June 21 (ca.

176 04h00 GMT) showed that weak Strombolian activity (Figs. 2a and 2b) was focused on a

177 narrow segment of the lower fractures and that a'a lavas had already attained the elevation of

178 1983 m asl (0.2 km before maximum runout, Fig. 2c). A small, weak gas plume was also

179 blowing northwards. A single sample of partially molten lava was collected from the still

180 active lava front and partially water quenched (Reu140621-1, Table S1, Fig. 2d). During most

181 of June 21, the activity consisted of lava effusion in three parallel lava streams (Fig. 2c)

182 merging in a single lava flow (Fig. 2e) and mild-weak "Strombolian" explosions at several

183 closely spaced spots along the lower part of the feeding fracture. At 13.00 (GMT), only weak

184 explosions were observed within a single small spatter cone (Figs. 2f and 2g). Most of the

185 lava field was formed of open channel a'a lavas. The total volume of lava was estimated by

186 MIROVA service (https://www.sites.google.com/site/mirovaweb/home), with the use of the

187 MODIS images and the analyses of the flux from the spectral properties, to be within 0.34 +/-

188 0.12 x 10^6 m^3, (Coppola et al., 2017). Satellite derived volume estimates are consistent with

189 independent photogrammetric estimates (0.4 ± 0.2 x 10^6 m^3; Peltier et al., 2016) and rank the

190 2014 eruption at the lower end of the volume range typically emitted by PdF (Roult et al.,

191 2012).

192 **3. Methodology**

193 **3.1 Sampling strategy**

194 Apart from the sample from the front of the still active lava flow (Fig. 2d), all other samples

195 were collected in two phases: 3 days after the eruption (pyroclasts on June 24, Fig. 3a; lavas

on July 2) and three months later (pyroclasts from the MV Fig. 1, on November 18) (Table S1). June 24 samples were collected both from the main fractures (WF and UF, Fig. 1a), the MV and the active lava flow (Fig. 1 and Table S1). Twenty five scoriaceous bombs and lapilli (REU140624-9a-1 to REU140624-9a and REU140624-9b-6 to REU140624-9b-25, in Table S3) were collected from the discontinuous deposit (Fig. 3d) emplaced at the WF site (Fig. 1a), active only at the beginning of the eruptive event. Because of the short duration of the activity at the WF, the scoria fragments on the ground were scarce (Fig. 3c). The strategy was to collect a sample that was formed by the largest available number of clasts that was representative of this discrete deposit (REU140624-9 in Table S1). From the Upper Fracture (UF in Fig. 1a) only one big scoria was collected (REU140624-13, Table S1) that broke in five parts, allowing us to measure its vesiculated core and the dense quenched external part (REU140624-13-a to REU140624-13-e, in Table S3). In contrast, the sustained and slightly more energetic activity at the lower tip of the fractures built a small spatter cone (Fig. 2) and accumulated a small volume continuous deposit (Fig. 3a) of inversely graded scoria fallout (Figs. 3b). This deposit is 10 cm thick at 2 m from the vent and covers an area of about ~1000 m^2 (Main Vent, MV, Fig. 1). For this fall deposit we collected two bulk samples, one from the base (within the lower 5 cm, REU141118-6 in Table S1) and the other from the top (within the upper 5 cm, REU140624-3, in Table S1), for the grain size and componentry analyses. The sample at the base was collected in November because on June 24 the loose proximal lapilli blanket was still very hot (405 °C; thermocouple measurement, Fig. 3a) and fumaroles with outlet temperatures in the range 305-60 °C were sampled all along the fractures several weeks after the eruption (Fig. 1b and Table S1). These latter geochemical data are not presented in this paper. We selected 103 fragments from the coarse grained bulk deposit at the top of the MV (REU140624-3-1 to REU140624-3-103, in Table S3) for density, connectivity, permeability, petrological and geochemical analysis. In addition, in November 2014, more than 200 clasts (comprising the REU141118-1 to REU141118-5 samples, Table S1) of similar size (maximum diameter between 16 and 32 mm, see Gurioli et al., 2015) were collected, both close to the MV and in the 'distal' area (30 metres away from the MVt) to complete the particle bulk texture analyses and the chemical analyses.

3.2 Grain size and componentry

We performed grain size analyses on the two bulk samples collected from the MV, following the procedure of Jordan et al. (2015) (Table S2). The samples were dried in the oven at 90°C and sieved at ½ phi intervals in the range of -5 φ to 4 φ (Fig. 3c); the data are also shown in

full phi for comparison with the deposits of the 2010 PdF fountaining episode (Hibert et al., 2015; Fig. 3f). Sieving was carried out by hand and for not longer than three minutes to avoid breaking and abrasion of the very vesicular and fragile clasts. For the scattered scoria sampled from the WF (Figs. 1, 3d and 3e), we followed the grain size strategy proposed in Gurioli et al. (2013). Within this procedure we sampled each fragment and we recorded the weight and the three main axes (a being the largest, b, and c). To allow comparison with the sieving grain size analyses (Inman, 1952), we used the intermediate b axis dimension to obtain $\varphi = -\log_2 b$.

Following the nomenclature of White and Houghton (2006) the componentry analysis is the subdivision of the sample into three broad components: i) juvenile, ii) non-juvenile particles, and iii) composite clasts. The juvenile components are vesicular or dense fragments, as well as crystals, that represent the primary magma involved in the eruption; non-juvenile material includes accessory and accidental fragments, as well as crystals that predate the eruption from which they are deposited. Finally, the composite clasts are mechanical mixtures of juvenile and non-juvenile (and/or recycled juvenile) clasts. In these mild basaltic explosions, the non-juvenile component is very scarce, so we focused on the juvenile component that is characterized by three groups of scoria: (i) spiny-opaque, (ii) spiny-glassy, and (iii) fluidal, along with golden pumice (Fig. 4). The componentry quantification was performed for each grain size fraction between -5 φ to 0.5 φ (Figs. 5a and 5b), where a binocular microscope was used for the identification of grains smaller than -1 phi (Table S2).

In the following, we will use the crystal nomenclature of Welch et al. (2009), with the strictly descriptive terms of macrocrysts (> 3 mm in diameter) mesocrysts (from 0.3 to 3 mm in diameter), and microcrysts (<0·3 mm in diameter). Regarding the June 2014 products, these ranges of size may however change in comparison to the December 2005 products studied by Welsch et al. (2009).

3.3 Particle bulk texture (density, porosity, connectivity, permeability) and microtexture

For each sample site (WF, UF and MV, Fig. 1a), we selected all the available particles within the 8-32 mm fraction for density/porosity, connectivity and permeability measurements (Table S3). This is the smallest granulometric fraction assumed to be still representative of the larger size class in terms of density (Houghton and Wilson, 1989; Gurioli et al., 2015), and has been used in previous textural studies (e.g., Shea et al., 2010). In addition, this size range is ideal for vesicle connectivity measurements (e.g. Formenti and Druitt, 2003; Giachetti et al., 2010; Shea et al., 2012; Colombier et al., 2017a, b). Density of juvenile particles was measured by the water-immersion technique of Houghton and Wilson (1989), which is based on

262 Archimedes principle. A mean value for the vesicle-free rock density was determined by

263 powdering clasts of varying bulk densities, measuring the volumes of known masses using an

264 Accupyc 1340 Helium Pycnometer, then averaging. The same pycnometer was also used to

265 measure vesicle interconnectivity for each clast using the method of Formenti and Druitt

266 (2003) and Colombier et al. (2017a). Permeability measurements were performed on five

267 clasts: two golden pumices, one fluidal, one spiny glassy and one opaque scoria, all collected

268 from the MV (Table S3). Following Colombier et al. (2017a), the clasts were cut into

269 rectangular prisms to enable precise calculation of the cross-sectional area, which is required

270 to calculate permeability. These prisms were then embedded in a viscous resin, which was left

271 to harden for 24 h. The sample surface had been previously coated with a more viscous resin

272 and then wrapped with parafilm to avoid intrusion of the less viscous resin inside the pores.

273 The coated samples were placed with a sample holder connected to a permeameter built in

274 Clermont-Ferrand following Takeuchi et al. (2008).

275   Vesicle size distribution was performed following the method of Shea et al. (2010) and

276 Leduc et al. (2015), while the total crystallinity, the percentages for both crystal phases

277 (plagioclase and clinopyroxene) and size-populations (meso and microcrysts) were calculated

278 using the raw data from FOAMS program (Shea et al 2010) and the CSDcorrections program

279 of Higgins (2000) and the CSDslice data base (Morgan and Jerram 2006) to have the

280 percentage in 3D. We performed these analyses on eight clasts picked up from each

281 component-density distribution (stars in Figs. 6a and 6b). The choice of the clasts was made

282 mostly on the typologies, rather than on each density distribution, in order to avoid the

283 analysis of clasts with transitional characteristics. For example, two golden pumice fragments

284 were selected from the largest clasts that were the less dense and didn't break, even if the

285 values in vesicularity were similar. A larger number of fluidal fragments were chosen (even if

286 the density distribution was unimodal) because this typology of clasts was the most abundant

287 and was emitted all along the active fracture, so we did our best in order to study products

288 representative of the WF, the UF and the MV activities. Only one spiny glassy and one spiny

289 opaque were selected, because they were emitted only at the MF. A full description of the

290 textural measurements all performed at Laboratoire Magmas et Volcans (LMV), as well as the

291 raw data of these measurements are available at DynVolc Database (2017).

292 **3.4 Bulk geochemistry**

293 For the determination of the bulk chemistry (Table S4 and Fig. 7) of the different pyroclasts

294 we selected the largest pyroclasts of golden pumice and the largest fluidal, spiny glassy and

295 spiny opaque scoriae (Table S4). We also analyzed two fragments of lava, from the beginning

296 and the end of the eruption (Table S4). Samples were crushed into coarse chips using a steel

297 jaw crusher and powdered with an agate mortar. Major and trace element compositions were

298 analyzed using powder (whole rock composition). In addition, for a sub-set of pyroclasts,

299 glass chips (2-5 mm in size) were hand-picked under a binocular microscope and analyzed

300 separately for trace elements. For major element analysis, powdered samples were mixed with

301 LiBO$_2$, placed in a graphite crucible and melted in an induction oven at 1050 °C for 4.5

302 minutes, resulting in a homogeneous glass bead. The glass was then dissolved in a solution of

303 deionized water and nitric acid (HNO$_3$), and finally diluted by a factor of 2000. The final

304 solutions were analyzed by ICP-AES. Trace element concentrations were analysed following

305 a method modified from Vlastélic et al. (2013). About 100 mg of sample (powder and chip)

306 were dissolved in 2 ml of 28M HF and 1 ml of 14M HNO$_3$ in teflon beaker for 36 hours at

307 70°C. Solutions were evaporated to dryness at 70°C. The fluoride residues were reduced by

308 repeatedly adding and evaporating a few drops of concentrated HNO$_3$, before being fully

309 dissolved in ca. 20 ml of 7M HNO$_3$. These solutions were diluted by a factor of 15 with

310 0.05M HF (to reach rock dilution factor of ca. 4000) and trace element abundances were

311 determined by quadrupole ICPMS (Agilent 7500). The analyses were performed in plasma

312 robust mode (1550 W). The reaction cell (He mode) was used to reduce interference on

313 masses ranging from 45 (Sc) to 75 (As). The signal was calibrated externally (every 4

314 samples) with a reference basaltic standard (USGS BHVO-2) dissolved as for the samples and

315 using the GeoRem recommended values (http://georem.mpch-mainz.gwdg.de/). For elements

316 that are not well characterized in literature (As, Bi, Tl), or which show evident heterogeneity

317 (e.g. Pb) in BHVO-2 powder, the signal was calibrated using the certified concentrations of a

318 synthetic standard, which was also repeatedly measured. The external reproducibility (2σ

319 error) of the method is 6% or less for lithophile elements and 15% or less for chalcophile

320 elements.

3.5 Glass and crystal chemistry

322 Spot analyses of matrix glass and crystal composition (Table S5) were carried out using a

323 Cameca SX100 electron microprobe (LMV), with a 15 kV acceleration voltage of 4 nA beam

324 current and a beam of 5 μm diameter for glass analyses. However, for the spiny opaque

325 scoria, characterized by abundant crystals with rapid growth textures, a voltage of 8 nA beam

326 current and a beam of 10 μm diameter were used. For this latter sample, 10 analyses per

327 sample were performed due to the heterogeneity within the highly crystallised glass (Fig. 8a),

328 while for the other samples 6 analyses per sample were enough to characterize the clean
329 homogeneous glass. For crystal analysis, a focused beam was used. For the characterization of
330 the meso- and micro-crysts, due to their small size, only two to three measurements were
331 performed, one at the edge, one in the middle and one at the core of the crystals, to check for
332 possible zonation.

3.6 Melt inclusions

334 Melt inclusions (MIs; Table S6, Figs. 8b and 9) were characterized in the olivine mesocrysts
335 from the three groups of scoriae (fluidal, spiny glassy and spiny opaque), but not in the
336 pumice group, because crystals were too rare and small to be studied for MIs.

337   Olivine crystals were handpicked under a binocular microscope from the 100– 250 and
338 250– 600 μm grain size fractions of crushed tephra. Crystals with MIs were washed with
339 acetone, embedded in epoxy and polished individually to generate adequate exposure of the
340 MIs for *in situ* electron probe microanalysis. The MIs are spherical to oblate in shape and
341 range in size from 10 to 200 μm. Some of the MIs contain shrinkage bubbles but all of those
342 studied are totally deprived of daughter minerals. Major elements were measured on a
343 Cameca SX-100 microprobe at LMV (Table S6). For major elements, the larger MIs were
344 analyzed with a spot diameter of 10-20 **μ**m and sample current of 8 nA, whereas the smaller
345 MIs were analyzed with a beam of 5 **μ**m and a sample current of 4 nA. The results are given
346 in Table S6, and analytical details and uncertainties are listed in Óladóttir et al. (2011) and
347 Moune et al. (2012).

4 Results

4.1 Deposit texture (grain size, componentry, morphology) and petrological description of the samples

351 The pyroclastic deposits at the WF and UF sites (Fig. 1a) are formed by scattered
352 homogeneous smooth fluidal (Figs. 3d) bombs and lapilli scoria. The average dimension of
353 the fragments is around 4 cm (maximum axis) with bombs up to 10 cm and scoria lapilli up to
354 2 cm in size.

355   At the MV, the reversely graded deposit is made up of lapilli and bombs, with only
356 minor coarse ash (Fig. 3c). The lower 5 cm at the base are very well-sorted and show a perfect
357 Gaussian distribution with a mode at 4 mm. In contrast, the grain size distribution of the upper
358 5 cm is asymmetrical with a main mode coarser than 22 cm and a second mode at 8 mm. This

359 upper deposit is negatively skewed due to the abundance of coarse clasts. The dataset shows a

360 similarity between the grain size distributions of the basal tephra ejected from the 2014 MV

361 and the ones for the lava fountaining of the 2010 summit event (Hibert et al., 2015). On the

362 contrary, the top of the 2014 fall differs from fountain deposits, being coarser and polymodal,

363 and it is ascribed to dominantly Strombolian activity.

364   In terms of componentry of the deposits, four types of clasts were distinguished (Fig.

365 4): (i) golden pumice, (ii) smooth or rough fluidal scoriae, (iii) spiny glassy scoria, (iv) spiny

366 opaque scoria. The pumices are vesicular, light fragments, characterized by a golden to light

367 brown color, sometimes with a shiny outer surface (Fig. 4a). They are usually rounded in

368 shape. Golden clasts studied for textures contain a few microcrysts of plagioclase (up to 0.1

369 mm in diameter), clinopyroxene up to 0.05-0.06 mm in diameter, and small olivine up to 0.03

370 mm in diameter (Fig. 4), together with large areas of clean, light brown glass. The fluidal

371 scoria fragments have dark, smooth or rough shiny surfaces (Fig. 4b). They can be more or

372 less elongated in shape and have spindle as well as flattened shapes. The fluidal fragments are

373 characterized by rare mesocrysts of plagioclase and clinopyroxene and microcrysts of

374 plagioclase, clinopyroxene and olivine (Fig. 4b). The spiny glassy fragments are dark, spiny

375 scoria that range in shape from subrounded to angular (Fig. 4c). These fragments contain

376 abundant glassy areas, while the spiny opaque fragments lack a glassy, iridescent surface.

377 Both groups of spiny clasts are characterized by the presence of dark and light brown glass.

378 The spiny opaque fragments are the densest fragments and have the largest amount of

379 crystals. They contain, as the most abundant phase, relatively large meso- and micro-crysts of

380 plagioclase, up to 3 mm long, together with meso- and micro-crysts of clinopyroxene and

381 olivine (Figs. 4c and 4d). In the dark portions of their matrix, tiny fibrous microcrysts of

382 olivine + clinopyroxene + plagioclase + Fe-Ti oxides occur. The spiny glassy fragments have

383 the same crystal populations as the spiny opaque ones, but their plagioclases are much smaller

384 and attain a maximum length of only 0.3 mm. Clusters of plagioclase and clinopyroxene are

385 present in both the spiny opaque and the spiny glassy fragments, as well as rare macrocrysts

386 of olivine. The olivine macrocrysts exhibit the typical compositional (Fo 84.2) and

387 petrographic features of olivine phenocrysts described in previous studies (Clocchiatti et al.,

388 1979; Albarede and Tamagnan, 1988; Bureau et al., 1998a and b; Famin et al., 2009; Welsch

389 et al., 2013). They are automorphic, fractured with oxides (mostly chromite) and melt

390 inclusions (Fig. 4c). Fluidal and pumice fragments studied for textures contain rare

391 macrocrysts and mesocrysts of olivine, and the crystals are essentially microlites. The pumice

392 and some fluidal fragments have lower contents of microlites than some fluidal and spiny

393   fragments, with the latter having the highest microlite content (Table S4). For comparison two
394   fragments of lava have been analyzed as well (Table S3). The lava fragments are poorly
395   vesiculated and completely crystalline (Fig. 4e). The lava contains the same paragenesis of
396   crystals described in the spiny opaque fragments, with the main difference that its matrix is
397   completely crystallized and constituted mostly by well-formed plagioclase up to 800 microns
398   and clinopyroxene up to 500 microns. Scarce, smaller olivines, are also present Ubiquitous
399   tiny rounded Fe-Ti oxides provide evidence of post emplacement crystallization.

400   The componentry results are reported in Figure 5 for the MV deposits; being the
401   deposits from the WF and UF characterized exclusively by fluidal clasts (Fig. 3). At the base
402   of the MV deposit, the coarse fraction of the deposit is rich in golden and fluidal components
403   that represent more than 60-70 vol% (Figs. 5a and 5b). The proportion of the two groups is
404   similar. In contrast, in the upper, coarse grained fall deposit, the clasts bigger than 8 mm are
405   dominated by the spiny scoria fragments, while the fraction smaller than 8 mm show a
406   dramatic increase in the golden and fluidal fragments, with the fluidal ones always more
407   abundant than the golden ones (Figs. 5a and 5b). Abundant light, golden, coarse lapilli pumice
408   and bombs have been found scattered laterally up to 30 metres from the main axis and were
409   not found in the proximal deposit. On the basis of the high amount of pumice in the lower part
410   of the deposit, we correlate the large, light clasts with the base of the proximal deposit, and
411   consequently we interpret them as material emitted at the beginning of the June 2014 eruptive
412   event.

413   **4.2 Particle density, porosity, connectivity, permeability and micro-texture**

414   Density analyses performed on 200 coarse lapilli reveal a large variation in density values
415   from 390 kg/m^{-3} to 1700 kg/m^{-3} with a median value at 870 kg/m^{-3} (Table S3). The fragments
416   collected from the MV have a bimodal density distribution, with a main population of light
417   fragments having a mode at 800 kg/m^{-3}, and a second and denser population centered at 1400
418   kg/m^{-3} (Fig. 6a). The golden and fluidal fragments form the lower-density population and the
419   spiny fragments are dominant in the denser population (Fig. 6a). For these samples there is a
420   marked correlation between porosity and morphology, so that the spiny-opaque clasts are the
421   densest (up to 1600 kg m^{-3}, with a vesicularity of 45 vol%) and the golden pumice are the
422   lightest (minimum density of 390 kg m^{-3} with a vesicularity of up to 86 vol%; with a Dense
423   Rock Equivalent density of 2.88 x 10^3 kg m^{-3}). The fluidal fragments collected at the WF (Fig.
424   1b), have a density range from 700 to 1400 kg/m^{-3} and a mode at 1000 kg/m^{-3} (Fig. 6b). The
425   five fragments from the only bomb collected at the UF are characterized by two distinct

426 density values, the low density one (700-800 kg/m^{-3}) refers to the core of the sample, while

427 the high density one (1400-1500 kg/m^{-3}) represents the quenched external rim of the bomb.

428 Finally, the two fragments of lava show the highest density values at 1800 and 2150 kg m^{-3}.

429 This last value is one of the highest found in the lava collected from 2014 up to 2017 (see Fig.

430 13 in Harris et al., 2017 and unpublished data)

431   In all these samples, the increase in vesicularity correlates with an increase in the

432 amount of small (0.1 mm), medium (0.5-1 mm) and large (up to 4 mm) vesicles. In the fluidal

433 clasts, these vesicles have a regular rounded or elliptical shape and are scattered throughout

434 the sample. The lightest pumices are often characterized by the presence of a single, large

435 central vesicle (10 – 15 mm) with the little vesicles and a few medium vesicles distributed all

436 around it (Fig. 4). The spiny glass texture is characterized by a lower amount of large vesicles

437 than in the pumice and by the presence of mostly medium sized vesicles, while the spiny

438 opaque has more irregular shape, very large (up to 10 mm) vesicles with a small and a

439 medium sized bubble population. In the spiny glass samples, the glass is more or less brown,

440 with the dark brown portions being the ones with the lowest vesicle content and the highest

441 microlite content. The opaque samples have a central, very dark glass portion, with low

442 vesicle content, and a more vesicular glassy portion at the outer edges (Fig. 4). The two

443 fragments of lava are poorly vesiculated (Fig. 6a) and characterized by large, irregular

444 vesicles (up to 5 mm in diameter). Clusters of small vesicles (up to 0.1 mm) are scattered

445 between the large ones.

446   The vesicle Size Distribution (VSD in Fig. 4) histograms picture well the decrease in

447 percentage of vesicles from the golden to the lava as well as the increase in coalescence and

448 or expansion in the spiny fragments, marked by the increasing of the large vesicles population

449 (Figs 4c and 4d). This trend is also marked by the decrease in number of vesicle per unit of

450 volume (N_v, Fig. 4) from the golden to the lava. Finally, the trend is also mirrored by the total

451 percentage of crystals (calculated in 3D, Fig. 4 and reported both in 3D and 2D for each

452 sample in Table S3) that increases with the increase of density of the clasts, from a minimum

453 of 8% in vol. for the golden up to 55 % in vol. for the spiny opaque scoria, and 100 % in vol.

454 for the lava (Fig. 4). Mesocrystals, formed mostly by the same proportion of plagioclase and

455 clinopyroxenes are absent or very scarce in the golden and fluidal fragments, while they reach

456 their maximum values, up 21% in vol. in the spiny opaque fragment. The population of

457 microcrystals is mostly constituted by plagioclases that range from a minimum of 6 % in vol.

458 in the golden, up to 23-25 % in vol. in the spiny fragments and to 64 % in vol. in the lava.

459   The connectivity data (Fig. 6c) also indicate that the fluidal and golden clasts have a
460   larger amount of isolated vesicles (up to 40% in volume) with respect to the spiny products.
461   The fluidal clasts from the WF are the most homogeneous with an average percentage of
462   isolated vesicles around 30% in volume. In contrast, both the pumice and the fluidal
463   fragments from the MV, characterized by higher values of porosity (> 75%), have a wide
464   range in percentage of isolated vesicles (between 20 and a few percentage in volume). The
465   fragments of the bomb collected at the UF are consistent with a vesiculated core characterized
466   by scarce isolated vesicles and the quenched rind that has 30 % of isolated vesicles. Finally
467   the spiny fragments have the lowest content of isolated vesicles (0-5% in volume). Despite the
468   presence of these isolated vesicles, all the samples shear high values of permeability (Fig. 6d).

4.3 Chemistry of the products

470   Major and trace element concentrations of whole-rock and hand-picked glass samples are
471   reported in Table S4. Whole rock major element composition is very uniform (e.g.,
472   6.5<MgO<6.7 wt%) and well within the range of Steady State Basalts (SSB), the most
473   common type of basalts erupted at PdF (Albarède et al., 1997). However, compatible trace
474   elements, such as Ni and Cr, are at the lower end of the concentration range for SSB
475   (<100ppm) indicating that the June 2014 eruption sampled relatively evolved melts. Ni and Cr
476   generally show higher concentrations in 2014 bulk rocks (79<Ni<92ppm and 71<Cr <87ppm)
477   compared to the 2014 glass chips (66<Ni<73ppm and 54<Cr <59ppm for all but two chips).
478   In the Cr vs Ni plot (Fig. 7a), whole rocks plot to the right of the main clinopyroxene +/-
479   plagioclase–controlled melt differentiation trend. This shift reflects the addition of Ni-rich
480   olivine (Albarède and Tamagnan, 1988). We estimate that the Ni excess results from the
481   occurrence of a low amount (0.7 to 1.3 wt%) of cumulative olivine in whole rocks, consistent
482   with thin section observations. The composition of olivine macrocrysts (ca. Fo84) is too
483   magnesian to be in equilibrium with the low-MgO evolved composition of the 2014 magma.
484   Using our estimate for the amount of cumulative olivine, we recalculate the olivine–corrected
485   MgO content of the 2014 magma at 6.2 wt%. The June 2014 melt is thus only moderately
486   depleted in compatible elements compared to the previous eruption of December 2010
487   (MgO~6.6 wt%, Ni~80 ppm, Cr~120 ppm). Conversely, the June 2014 melt is significantly
488   depleted in compatible elements compared to the earlier November 2009 eruption, which
489   sampled relatively primitive magmas (average MgO~7.7 wt%, Ni~135 ppm, Cr~350 ppm)
490   (Fig. 7a). The 2014 evolved composition plots at the low-Ni-Cr end of PdF historical
491   differentiation trend (Albarède and Tamagnan, 1988), near the composition of lavas erupted

492   on 9 March 1998 after 5.5 years of quiescence (1992-1998). Note that olivine accumulation at

493   PdF generally occurs in melt having ca.100 ppm Ni (Albarède and Tamagnan, 1988). Olivine

494   accumulation in evolved melts (Ni < 70 ppm) seems to be a distinctive feature of many small

495   post-2007 eruptions (e.g. this event and the three 2008 eruptions, see Di Muro et al., 2015).

496   A closer inspection of Ni-Cr variability in June 2014 whole rock samples (Fig. 7b)

497   reveals that scoria from the Western Fracture (140624-9b-6, Table S4) and early erupted lavas

498   (1406-21-1, Table S4) have the lowest amount of olivine (<0.9%) whereas scoria from the

499   Upper Fracture (140624-13a) and late erupted lavas (140324-12) have a slightly higher

500   amount of olivine (>1.2%). This is consistent with the general trends observed at PdF of

501   olivine increase from the start to end of an eruption (Peltier et al., 2009).

502   The so called "olivine control trend" in Ni-Cr space cannot be explained either by

503   addition of pure olivine (which contains less than 500 ppm Cr (Salaün et al., 2010; Di Muro et

504   al., 2015; Welsch et al., 2009), or by the addition of olivine plus pyroxene (which would

505   require ca. 50% pyroxene with 970 ppm Ni and 4800 ppm Cr, see Fig. 7 caption). Instead,

506   addition of olivine hosting ca. 1% Cr-spinel (with 25 wt.% Cr) accounts for data and

507   observations, and is consistent with crystallization of olivine and Cr-spinel in cotectic

508   proportions (Roeder et al., 2006). The fact that some samples (golden pumice) plot off the

509   main, well-defined array, can be explained either by addition of more or less evolved olivine

510   crystals (within the range of Fo 80-85 measured in June 2014 samples) and/or slight

511   variations (± 0.02%) in the proportion of Cr-spinels (Fig. 7b).

512   The glass chemistry of the four clast types allows us to correlate porosity and oxide

513   contents and shows an increase in MgO from the spiny opaque to fluidal and golden

514   fragments (Fig. 8a). Consistent with petrological and textural observations, the spiny opaque

515   is the most heterogeneous type of clast in terms of glass composition (Fig. 8). The glassy

516   portion at the edge of the clast is similar to the spiny glass, while the interior, characterized by

517   dark areas rich in tiny fibrous microcrysts, shows scattered glass compositions with very low

518   MgO content as well as a decrease in CaO (Fig. 8). We attribute the significant variation in

519   glass composition within the different components to variable degrees of micro-crystallisation

520   as the bulk chemistry of all clasts is very similar and globally homogeneous.

521   **4.4 Melt inclusions**

522   MI analyses must be corrected for post-entrapment host crystallisation at the MI - crystal

523   interface. We used a Kd = $(FeO/MgO)_{ol}$ / $(FeO/MgO)_{melt}$ = 0.306 (Fisk et al., 1988; Brugier,

524 2016) and an average $Fe^{3+}/\Sigma Fe_{total}$ ratio of 0.11 (Bureau et al., 1998a; Di Muro et al., 2016 and

525 references therein) defined for PdF magmas. For the June 2014 melt inclusions, the post

526 entrapment crystallization (PEC) ranges from 2.9 to 10.5 wt%. Raw and corrected major and

527 volatile element concentrations of MIs are reported in Table S6.

528   Host olivines span a large compositional range from Fo_{80} to Fo_{86}. Despite the evolved

529 bulk composition of the magma, most olivines are quite magnesian (Fo_{83-85}) and are not in

530 equilibrium with the evolved host magma. On the contrary, Mg-poor olivines (Fo_{80-81}) can be

531 considered as being in equilibrium with the bulk rock composition. The corrected

532 compositions of MIs in phenocrysts from the different samples partly overlap with the

533 evolved bulk rocks (MgO_{wr}: 6.1-7.2 wt%) and extend to higher MgO contents of up to 8.8

534 wt% (Table S6). MIs display a narrow range of transitional basaltic compositions (K_2O= 0.5-

535 0.9 wt%) and show no significant difference between the three types of scoriae. The major

536 element composition of melt inclusions correlates with that of the host olivines. Melt

537 inclusions in the high Fo-olivines have the highest MgO, CaO and TiO_2 and lowest K_2O

538 concentrations (Table S6). It is interesting to note that the June 2014 products contain two

539 populations of magnesian ($Fo_{>83}$) olivines hosting melt inclusions with two distinct Ca

540 contents. Most of the magnesian olivines contain MIs with unusually high CaO contents (11.6

541 – 12.9 wt%) and high CaO/Al_2O_3 ratios (0.8-0.9), higher than that of the bulk rocks (0.8) (Fig

542 8). The occurrence of olivines with "high Ca" melt inclusions has been observed in all three

543 different types of scoriae. A few magnesian olivines and all Mg-poor olivines ($Fo_{80.5-83.6}$) host

544 MIs with lower CaO contents (11.4 wt%). This latter composition overlaps with that of the

545 bulk rock (Fig 8). The "high Ca" population of inclusions is also enriched in TiO_2 and Al_2O_3

546 and depleted in MgO, FeO_T and Na_2O for a given olivine Fo content with respect to the "low

547 Ca" population. Both low- and high-Ca populations of melt inclusions have similar K_2O

548 contents and total alkali content increases from 3 wt% at 12.6 wt% CaO, to 3.5 wt% at 10.8

549 wt% CaO. However, we remark that high Ca melt inclusions from the June 2014 activity

550 record a significant scattering in K_2O contents, which range from 0.55 to 0.9 wt%. These

551 anomalous compositions potentially track processes of crystal dissolution (e.g. pyroxene

552 dissolution).

553   MIs in olivines from June 2014 can best be compared with those of other recent small-

554 volume and short-lived eruptions which emitted basalts with low phenocryst contents, like

555 those in March 2007 (0.6 x 10^6 m^3) and November 2009 (0.1 x 10^6 m^3) (Roult et al., 2012).

556 March 2007 aphyric basalt has a bulk homogeneous composition with intermediate MgO

557 content (MgOwr: 7.33 wt%; K_2O: 0.67 wt%). Their olivines (Fo 81) are in equilibrium with

558 the bulk rock and their composition is unimodal (Di Muro et al., 2014). November 2009

559 products are the most magnesian lavas emitted in the 2008-2014 period, slightly zoned

560 (MgOwr: 7.6-8.3 wt%; K_2O: 0.75 – 0.62 wt%) and contain a few percent of normally zoned

561 olivine macrocrysts with bimodal composition (Fo81 and Fo83.5, see Di Muro et al., 2016).

562 June 2014 bulk rocks (MgO_{wr}: 6.7 wt%; K_2O: 0.75 wt%) and melt inclusions in Fo_{80-81}

563 olivines are quite evolved. Their composition is close to that of products emitted by summit

564 intracaldera eruptions in 2008, ca. 1.5 years after the large 2007 caldera forming eruption (Di

565 Muro et al., 2015) (Fig. 8). As already reported for 2008 products, many olivine macrocrysts

566 of 2014 are clearly too magnesian to be in equilibrium with the relatively evolved host melts.

567 Overall, MgO content in 2007-2014 melt inclusions tends to decrease with decreasing Fo

568 content of the host olivines. MIs in olivines also exhibit a trend of linear decrease in MgO and

569 increase in FeO from April 2007 to 2009-2014 products (Fig. 9). Melt inclusions in March

570 2007, November 2009 and June 2014 follow the same trend of FeO enrichment (Fig. 9). In the

571 large-volume and olivine-rich April 2007 products, MIs in magnesian olivines with $Fo_{>82}$ have

572 distinctly higher MgO, FeO and lower SiO_2 and Al_2O_3 than MIs in 2009-2014 products. The

573 distinctive FeO enrichment of many of the MIs from the April 2007 oceanite has been

574 interpreted by Di Muro et al. (2014) as a result of post-entrapment modification related to new

575 magma inputs into long lasting magma storage.

576 Two populations of low- and high-Ca melt inclusions are also found in the November

577 2009 olivines. Low-Ca melt inclusions from the November 2009 and June 2014 eruptions

578 indicate a single trend of chemical evolution (Fig. 8), consistent with bulk rock compositions.

579 June 2014 products have lower MgO and CaO contents than those from November 2009.

580 Significant scattering in K_2O content (0.6-0.9 wt%) is found in low-Ca inclusions from 2009,

581 as observed in high-Ca inclusions from the 2014 eruption, but they share similar K_2O

582 contents. In 2009 and 2014 products, K_2O content of melt inclusions is partly anti-correlated

583 with the olivine Fo content. This observation has been attributed to moderate heterogeneity of

584 primary melts feeding the plumbing system of PdF. Rapid temporal changes of K_2O content in

585 PdF basalts have been reported (Boivin and Bachelery, 2009).

586 **4.5 Mineral composition and glass – plagioclase equilibrium**

587 All 2014 scoriae (spiny, fluidal, golden) contain the same paragenesis of olivine,

588 clinopyroxene and plagioclase. The composition of minerals found in golden, fluidal and

589 spiny scoriae is indistinguishable.

590   In olivines, average MgO content decreases from macrocrysts ($Fo_{84.1}$) to mesocrysts

591   ($Fo_{79.6}$) to microlites. Olivine microlites (Table S5) are normally zoned. Their composition

592   ranges from $Fo_{78.0-75.3}$ in the cores to $Fo_{74.3-70..5}$ in the rims. Overall, olivines in 2014 products

593   span the full range of typical Fo contents of recent PdF magmas (Boivin and Bachèlery, 2009;

594   Di Muro et al., 2014; 2015). Clinopyroxene composition (augites) ranges from $En_{53}Fs_{15}Wo_{32}$

595   to $En_{41}Fs_{14}Wo_{45}$. Their average composition ($En_{45}Fs_{14}Wo_{41}$) is consistent with that found in

596   other recent evolved melts like those emitted by the 2008 eruptions (Di Muro et al., 2015) and

597   more generally in recent PdF products (Boivin and Bachèlery, 2009). Clinopyroxenes are

598   unzoned, the composition of cores and rims is very similar and close to that found in

599   microcrysts and mesocrysts. Plagioclase composition ranges from $An_{79.5}Ab_{19.9}Or_{0.6}$ to

600    $An_{63.1}Ab_{35.7}Or_{1.2}$ with a bimodal distribution ($An_{76.5-79.5}$ and $An_{63.1-72.9}$, Fig. 10a). Similar

601   bimodal distributions were observed in many other products, at PdF (Di Muro et al., 2015).

602   Mesocrysts ($An_{75.5}Ab_{23.8}Or_{0.7}$ on average) are more calcic with respect to microcrysts

603   ($An_{65.7}Ab_{33.1}Or_{1.2}$ on average). Normal zoning is found from plagioclase cores to rims (Fig.

604   10a). The composition and zonation of 2014 plagioclases clearly contrast with the complex

605   and often reverse zoning patterns and intermediate composition of the 2008 PdF products that

606   were attributed to pre-eruptive magma heating (Di Muro et al., 2015).

607   Plagioclase-melt equilibrium and melt composition in pyroclastic rocks and water-

608   quenched lavas were used to estimate both temperature and water content dissolved within the

609   melt (Fig. 10b and Table S5). Temperature estimates are based on the (dry) equation of Helz

610   and Thornber (1987) recalibrated by Putirka (2008). Dissolved water content was calculated

611   from the plagioclase hygrometer of Lange et al. (2009) at 50 MPa. This pressure corresponds

612   to the average CO_2-H_2O saturation pressure (recalculated with Papale et al., 2006) typically

613   recorded in melt inclusions from central products at PdF (e.g. 1931 eruption in Di Muro et al.,

614   (2016) and references therein). This pressure roughly corresponds to the sea level depth,

615   which is inferred to be the location of the potential main shallow magmatic reservoir (Peltier

616   et al., 2009; Lengliné et al., 2016; Coppola et al., 2017). The application of the plagioclase

617   hygrometer of Lange et al. (2009) makes it possible to estimate the dissolved water content in

618   the melt with a nominal uncertainty of 0.15 wt% and is only slightly dependent on pressure.

619   Plagioclase compositions not in equilibrium with the melt (glass or bulk rock) are those of

620   mesocryst cores with the highest ($An_{>76.5}$) anorthite content (Fig. 10a and Table S5). Such

621   compositions are more in equilibrium with CaO-richer magnesian melts than those measured

622   in matrix glasses and bulk rocks of 2014 eruption and likely formed during early stages of

623   shallow magma differentiation (Fig. 10a).

624   In order to determine pre-eruptive conditions, calculations were performed only on

625   paired plagioclase rims and matrix glasses in equilibrium, using the plagioclase-melt

626   equilibrium constant of Putirka (2008) calibrated for melts whose temperature exceeds

627   1050°C ($Kd_{An-Ab} = 0.27\pm0.05$). Our review of published and unpublished data shows that melt

628   temperature progressively decreases from April 2007 (1188+/-16 °C) to January-October

629   2010 (1147+/-9°C) and positively correlates with K_2O content in melts which increases from

630   0.70 to 0.96 wt% (Fig. 10b). The melts from the June 2014 eruption record the lowest

631   temperatures in post-2007 eruptions (1131±15 °C) together with the highest K_2O-enrichment

632   (K_2O: 0.90±0.12 wt%). The lowest temperatures are recorded by spiny scoriae, while the

633   temperature of golden scoriae overlaps with that of 2010 products emitted before the 2010-

634   2014 phase of quiescence. In spite of the large variability in melt composition and

635   temperature, average pre-eruptive water content dissolved in the melts (0.5 +/- 0.2 wt%) is

636   quite homogeneous for the whole 2008-2014 period. In 2014, the lowest estimated dissolved

637   water content (down to 0.38 wt%) is for the golden and some fluidal scoriae, while the

638   maximum amount (0.68 wt%) is for the spiny opaque scoriae. However, water content

639   estimated from core-bulk rock equilibrium (0.3±0.1 wt%) is slightly lower than that estimated

640   from rim and microlite-matrix glass equilibrium (0.5±0.2 wt%), but the difference broadly

641   overlaps the nominal uncertainty related to calculations. Dissolved water contents in melts of

642   the pyroclasts are thus intermediate between those measured in 2007 melt inclusions (H_2O:

643   0.8 +/- 0.15 wt% and up to 1.1 wt%) and those typically found in degassed matrices of lava

644   and Pele's hairs of 2007 (Fig. 10; 0.2 wt%; see Di Muro et al., 2015; 2016).

645   **5 Discussions**

646   **5.1 Eruptive dynamics**

647   The activity fed by the uppermost WF and UF (Fig. 1) was very short-lived, as shown by the

648   presence of only scattered bombs and coarse lapilli (Figs 3d and 3e). The homogeneity of

649   these clasts, their coarse grained nature and the fluidal smooth texture are in agreement with

650   very short-lived fire-fountaining/magma jets. Glassy outer surfaces of clasts have been

651   interpreted as a late-stage product of fusion by hot gases streaming past the ejecta within the

652   jet/fountain (Thordarson et al., 1996; Stovall et al., 2011). However, the occurrence of this

653   process is not supported by the homogeneous glass composition in our fluidal clasts.

654   Therefore, we interpret these features here just as rapid quenching and not re-melting.

655   Vlastélic et al. (2011) have documented the mobility of alkalis and other elements on PdF

clasts that experienced long exposures to acid gases. In the 2014 eruption pyroclasts, the mobility of elements is prevented by the short duration of the events.

At lower altitude and close to the MV (Fig. 1), the 5 cm layer at the base of the fall deposit is fine-grained (Figs. 3b and 3c), rich in fluidal and golden fragments (Fig. 5), with a perfect Gaussian grain size curve (Fig. 5), and similar to that reported from the weak 2010 fountaining event (Fig. 3f and Hibert et al., 2015). Therefore, we interpret this deposit as being due to weak Hawaiian like fountaining (sustained, but short-lived) activity. We want to remark here that this activity happened during the night and was not observed. The top of the same deposit is coarse grained (Figs 3b and 3c), bimodal, has a lower content in coarse ash (Table S2) and is rich in spiny opaque and spiny glass fragments (Fig. 5). The reverse grain size likely records the transition from early continuous fountaining to late discrete Strombolian activity (observed and recorded on the 21 of June 2014, Fig. 2). This transition in activity is typical of many eruptions at PdF (Hibert et al., 2015). The reverse grading of the whole deposit (Figs. 3b and 3c) is thus not correlated with an increase in energy of the event, but with two different eruptive dynamics and fragmentation processes. The decrease in coarse ash, which correlates with the decrease in energy of the event, highlights the most efficient fragmentation process within the Hawaiian fountaining with respect to the slow gas ascent and explosion of the Strombolian activity. These conclusions are consistent with (i) the continuous and progressive decrease in intensity of Real time Seismic Amplitude Measurement recorded by the OVPF seismic network (unpublished data), and (ii) satellite derived TADR which suggest continuous decay of magma output rate after an initial short-lived intense phase (Coppola et al., 2017).

5.2 Interpretation of the different textural signatures and the meaning of the 4 typologies of clasts.

1) *Background on the texture of clasts from Hawaiian and Strombolian activities*

The first microtextural analysis of Hawaiian ejecta was performed by Cashman and Mangan (1994) and Mangan and Cashman (1996) on pyroclasts from 1984 to 1986 Puʻu ʻŌʻō fountainings. The authors defined two clast types: 1) 'scoria' consisting of closed-cell foam of ≤85% vesicularity, with round, undeformed, broadly-sized vesicles, and 2) 'reticulite', an open-cell polyhedral foam with ~1 μm thick vesicle walls with >95% vesicularity. They stated that the scoria to reticulite transition is a consequence of Ostwald ripening, where larger bubbles grow at the expense of smaller bubbles due to post-fragmentation expansion of clasts

688 within the fountain. According to this model, scoria preserves textures closer to conditions at

689 fragmentation, whereas continued vesiculation and clast expansion in the thermally-insulated

690 core of the fountain results in reticulate. This model was confirmed at lava fountains at Etna

691 (Polacci et al., 2006), Villarrica (Gurioli et al., 2008), Kīlauea Iki, (Stovall et al., 2011 and

692 2012), Mauna Ulu (Parcheta et al., 2013) and Al Madinah (Kawabata et al., 2015). These last

693 authors also measured the connected and isolated porosity in the AD1256 Al-Madinah

694 Hawaiian fountaining eruptions. They found that the reticulite-like textures from the central

695 part of these very high fountains showed isolated vesicles in agreement with low shear rates

696 and low viscosity melts, where bubbles may grow spherically and remain isolated. In contrast,

697 at margins of the fountains, high shear may lead to stretching and mechanical coalescence of

698 bubbles, forming the common, fluidal types of particles seen also in the deposits. They also

699 stated that lower vesicularity and greater isolated porosity were found in some tephra

700 interpreted as resulting from violent Strombolian eruptive phases.

701 The data that we found in our study of the typical activity of PdF agree only partially

702 with all these interpretations. The reason is that we sampled and measured products of very

703 weak Hawaiian to Strombolian activities. If we plot the approximate durations and masses of

704 these events on the Houghton et al. (2016) diagram, the 2014 activity of PdF falls into the two

705 fields for transient and fountaining activity, but at the base of the diagram. We here show for

706 the first time that short lived and weak fountaining can preserve pyroclast textures that record

707 magma ascent and fragmentation conditions before the explosions and also provide some

708 information about the pre-eruptive storage conditions. The occurrence of time-variable ascent

709 conditions is also reflected in the time evolution of eruptive dynamics, with the golden and

710 fluidal scoriae emitted from the low Hawaiian fountaining episodes and the spiny fragments

711 from the Strombolian-like explosions

712 *2) The four typologies of clasts and their distribution in space and in time in the 2014*

713 *eruption at PdF*

714 So, as described in 5.1, longitudinal variation in eruptive style along the fracture system

715 produces a spatial variability in the proportions of the four typologies of clasts. The

716 uppermost fractures (Western and Upper Fractures, Fig. 1a) are characterized solely by fluidal

717 fragments (Fig. 4b); they lack both the spiny and the golden components. In addition, these

718 fluidal clasts are the ones showing the smoothest surfaces (indicative of rapid quenching in a

719 very hot environment), low porosity values (between 50 to 77%, Fig. 6b), the highest content

720 in isolated vesicles (~ 30% in vol. Fig. 4c), and low vesicle numbers (3 to 5 x 10^6, Fig. 4b),

comparable to the spiny fragments. They have scarce mesocrysts (1-2 % in vol. Table S3) and very low amount of microcrysts of plagioclase and clinopyroxene (3 to 11 % in vol., Table S3). These fluidal scoria fragments were emitted by short lived jets of magma, therefore they underwent rapid quenching in a very hot environment that prevented any expansion or further vesiculation and preserved a very high number of isolated vesicles (Fig. 6d). Syn-eruptive crystallization was hindered by high ascent velocities in the dyke, due to the sudden release of over-pressure in the shallow magma reservoir.

The four typology of clasts, golden pumice, fluidal scoria and the spiny fragments (Fig. 4), were found associated only at the MV. The proportion of these fragments correlate with the eruptive dynamics, being the golden lapilli and fluidal clasts dominant in the Hawaiian, more energetic activity at the beginning of the eruption (during the night between the 20 and the 21 of June 2014) and the spiny fragments dominant during the Strombolian activity, coinciding with the decreasing in Mass Discharge Rate (MDR, early in the morning of the 21, Fig. 2 and Coppola et al., 2017). The golden and fluidal fragments from the MV show the highest porosity (86 %, Fig. 6a), variable proportions of isolated vesicles (Fig. 6c) and high, but variable, N_V numbers (Figs. 4a). They are also characterized by a uniform vesicle size population with clear evidence of incipient expansion, especially in the fluidal fragments (Figs. 4a and 4b). From the connectivity graph, there is a clear decrease in isolated vesicles with the increase in vesicularity (Fig. 6c). The content in crystal, mostly formed by microcrysts of sodic plagioclase (Fig. 10a) due to magma degassing during its ascent and decompression in the conduit (Di Muro et al., 2015), is very low, especially in the golden pumice (up to 15% in vol.), and slightly higher for the fluidal clasts (up to 23 % in vol.). We interpret the golden fragments, at the MV, to be the fastest (low amount of microcrysts) and less degassed magma (high vesicularity coupled with high N_V), which experienced only a very short residence time in the magma transport system (dyke+vent), followed by the fluidal fragments. In contrast the spiny fragments, characterized by higher percentage of microcrysts and mesocrysts, by the lack of isolated vesicles, by the presence of coalescence signature and low N_V values (Figs. 4c and 4d), are indicative of an extensively degassed and cooled magma. The presence of the mesocrysts (that formed in the shallow reservoir) in the spiny fragments, and their slightly cooler temperature (Fig. 10b), strongly support this interpretation. The spiny fragments likely record the slowest ascent velocity and the longest residence time in the reservoir+dyke+vent system compared to the golden/fluidal counterpart. Therefore these fragments are associated with Strombolian events, and decreasing MDR, in agreement with their slower ascent that allows extensive syneruptive crystallization.

755   Among spiny fragments, the opaque ones are the densest, they lack a uniform glassy

756   surface, and they are characterized by i) very high microlite content, ii) strong coalescence

757   signature (Fig. 4d), iii) heterogeneous glass chemistry, and iv) mingling with hotter magma at

758   the clast edges (Fig. 8a). All these features reveal the composite nature of these clasts. We

759   interpret the spiny opaque as spiny glass fragments recycled inside the eruptive vent during

760   the explosions, being the densest portion of the magma prone to fall back in the vent/fracture

761   (Fig. 2b).

762

763   *3) Degassing-driven versus cooling-driven crystallization*

764

765   Syn-eruptive degassing is favoured by bubble connectivity/permeability in the ascending

766   magma, enhanced by syn-eruptive crystallisation in the conduit (especially microcrysts of

767   plagioclase, Fig. 10a), even for magmas at low vesicularity. However, our dataset also support

768   the occurrence of magma stratification in the reservoir. Textural and petrological data

769   demonstrate that the initial activity emitted a small volume of melt (represented by golden and

770   large part of the fluidal fragments) with very scarce crystals. This crystal-poor melt was

771   followed in time by the main volume of magma that contains a larger amount of mesocrysts

772   (spiny clasts and lava). Lava flows represent the main volume emitted in the 2014 eruption.

773   Mesocrysts are absent in the golden, scarce in the fluidal and more abundant in the spiny (Figs

774   4b, 4c and 4d) and lava (Fig. 4e) and consist in an equal percentage of plagioclase and

775   clinopyroxene and minor olivine. Their composition indicate that they formed in the reservoir,

776   as shown by their different composition in respect to the microcrysts counterparts (Fig. 10a)

777   that formed during melt degassing in the conduit. Most important, a large amount of

778   microcrysts in lava formed in the reservoir as well during magma cooling (Figure 10a). So,

779   we have a range of crystallization conditions. The fact that the lighter plagioclase are not

780   concentrated in the upper and early erupted portion of the reservoir can be due either to the

781   fact that often they are locked in clusters with the clinopyroxene or that this melt was expelled

782   from the crystal-rich portion of the reservoir (see Figure 10b). Water exsolution from the melt

783   can result from its extensive crystallization, which induces an increase in dissolved volatile

784   content, up to saturation (second boiling) and can drive melt-crystal separation.

785   In conclusion, the crystals in the 2014 fragments do reflect the shallow reservoir

786   conditions and the ascent degassing processes.

787

788   *4) Textural syn-eruptive versus post fragmentation modifications*

790   To prove that the 2014 vesiculation of the clasts have been not modified by post

791   fragmentation expansion process, following Stovall et al. (2011), we use a plot of vesicle-to-

792   melt ratio (V_G/V_L, after Gardner et al., 1996) and vesicle number density (N_V, Fig. 11). As

793   demonstrated by Stovall et al. (2011), addition of small bubbles leads to an increase in N_V and

794   only a slight increase in V_G/V_L. Bubble growth by some combination of diffusion and

795   decompression leads to an increase in V_G/V_L at constant N_V. N_V decreases while V_G/V_L

796   increases during bubble coalescence, whereas loss of bubbles via collapse or buoyant rise

797   leads to a reduction in both parameters. Intermediate trends on the diagram reflect

798   combinations of more than one of these processes. The pumice and the scoria from the MV of

799   PdF show the highest V_G/V_L, but also the highest Nv, suggesting preservation of small

800   vesicles and growth by some combination of diffusion and decompression. The presence of

801   the small vesicles and the lack of a strong coalescence/expansion signature confirm that the

802   weak PdF activity leads to only limited post-fragmentation expansion inside the hot portions

803   of the short-lived fountains. These data contrast with the data from the more energetic

804   fountaining events observed at Kilauea or elsewhere, where pre-eruptive information is

805   basically erased because pumice textures are dominated by expansion effects due to their

806   longer residence within the long-lived energetic fountaining. In contrast, the densest, spiny

807   scoriae and the scoria from the Fractures activity show the lowest values of Nv and V_G/V_L,

808   due to incipient coalescence and/or loose/lack of small bubbles.

809   According to previous works (listed above), the golden pumice of PdF should be

810   derived from the central part of the fountains, but they do not show the strong post expansion

811   signatures reported in the literature (Fig. 11). It is interesting to note that the fluidal fragments

812   at the MV are less smooth (Fig. 4), more vesiculated, and have a lower content of isolated

813   vesicles than the fluidal scoria from the uppermost Fractures (Fig. 6). Therefore fluidal

814   fragments at the 2014 MV could indeed represent clasts that have been partly modified during

815   their residence in the external part of the fountains, while the golden samples could come

816   from the central part (Stovall et al., 2011 and 2012). However, the slight differences in

817   crystallinity and glass chemistry between the fluidal and golden fragments support the idea

818   that each of these fragments has an imprint from the pre-fragmentation setting. In contrast, the

819   spiny fragments from the MV and the fluidal fragments from the Fractures show low N_V and

820   low V_G/V_L in agreement with loss of vesicles and coalescence. However, the presence of large

821   numbers of isolated vesicles within the fluidal scoria from the Fractures agrees with their

822   provenance from a fast hot ejection of relatively degassed magma (low N_V). In contrast the

823 spiny fragments, especially because of the presence of abundant mesocrysts and increase in
824 syneruptive microcrysts, are indicative of the slowest ascent velocity and extensively
825 degassing and cooled magma. The spiny fragments are the most degassed, densest and the
826 most crystal rich magma that was emitted during low-energy activity by Strombolian
827 explosion, where recycling phenomena were also very frequent (Fig. 2f).

828 Our vesicle connectivity results are in full agreement with the recent review of
829 Colombier et al. (2017b). According to these authors, connectivity values can be used as a
830 useful tool to discriminate between the basaltic scoria from Hawaiian (fire fountaining) and
831 Strombolian activity. The broad range in connectivity for pumice and scoria from fire
832 fountaining is interpreted simply as being due to variations in the time available before
833 quenching due to differences in location and residence time inside the fountain. The fluidal
834 fragments from the WF are the richest in isolated vesicles because they are transported by
835 very short lived hot lava jets. In contrast, the higher connectivity observed in scoria from
836 Strombolian activity is probably related to their higher average crystallinity, and more
837 extensive degassing prior to the eruption, (Colombier et al., 2017b). The spiny surface of
838 these Strombolian fragments is due to the fact that these weak explosions emit only a small
839 solid mass fraction and the partially quenched dense clasts land quickly after a short cooling
840 path through the surrounding atmosphere (e.g. Bombrun et al., 2015).

841 All the clast, from golden to spiny, are very permeable, independent on their
842 vesicularity, crystal content and/or of the presence of isolated vesicles. This is in agreement
843 with our interpretation that magma degasses during its ascent in the conduit and that promotes
844 microlite nucleation (see the sodic plagioclase, Fig. 10a) before magma fragmentation (see
845 also Di Muro et al. 2015 with the Pele's hairs ad tears samples for the three 2008 eruptions).
846 Moreover, we always find that some of the spiny clasts (especially the opaque ones) are
847 slightly less permeable that the golden and fluidal ones, but not as impermeable as we would
848 expect by their low vesicularity.

849 In conclusion, we can state that i) the crystals lower the percolation threshold and
850 stabilize permeable pathways and ii) this is true for the syn-eruptive sodic plagioclase that
851 favor an efficient degassing in the relatively crystal-rich magma, because of their low wet
852 angles that favor degassing against nucleation (Shea, 2017) and their aspect ratio (e.g. Spina
853 et al. 2016) iii) therefore permeability develops during vesiculation through bubble
854 coalescence, which allows efficient volatile transport through connected pathways and
855 relieves overpressure (Lindoo et al., 2017). Pervasive crystal networks also deform bubbles
856 and therefore enhance outgassing (Oppenheimer et al., 2015). Based on Saar et al. (2001)

crystals should start to affect the behavior of the exsolved volatile phase when they approach 20 vol% (Lindoo et al., 2017). In our dataset, apart from the golden and part of fluidal, all the other clasts do have microlites >20%. Our data completely support that slow decompression rate allows more time for degassing-induced crystallization, which lowers the vesicularity threshold at which bubbles start to connect.

Rapid re-annealing of pore throats between connected bubbles can happen due to short melt relaxation times (Lindoo et al; 2016). This phenomenology could explain the high amount of isolated vesicles in the fountaining samples. However, vesicle distributions of the golden and fluidal fragments are almost perfect Gaussian curves, so it seems that if the relaxation process happens it just merged perfectly with the expected vesicle distribution. In contrast, coalescence and/or expansion (as we observe in the spiny fragments) do not fit the curves (Fig. 4). In addition, we should expect that in crystal-poor fragments, due to melt relaxing and pathways closure, the clasts became impermeable after quenching, as revealed by some petrological experiments performed on crystal-poor basaltic magma (Lindoo et al., 2016). In contrast, in high crystalline magmas, the presence of micro-crystals increases viscosity thus preserving the coalesced textures (see Moitra et al., 2013). The isolated vesicle-rich fragments of the 2014 PdF eruption are highly permeable, and are characterized by variable ranges of porosity and numbers of vesicles (Fig.4 and Fig. 6d) that seem more related to the pre-eruptive conditions than to the post relaxation of low-viscosity melts. In the 2014 crystal-poor samples, the permeability increases rapidly once the percolation threshold has been reached, and efficient degassing prevents bubble volumes from expanding past the percolation threshold (Rust and Cashman 2011).

5.4 Integration between the physical and textural characteristics of the products and their geochemical signature: insight into the feeding system

According to Peltier et al. (2016), the June 2014 eruption emitted magma from a shallow pressurized source located only 1.4-1.7 km below the volcano summit. Coppola et al. (2017) suggest that the 2014 event was fed by a single shallow and small volume magma pocket stored in the uppermost part of the PdF central plumbing system. All 2014 clasts show homogeneous and evolved bulk compositions, irrespective of their textural features. June 2014 products are among the most evolved products erupted since at least 1998 and are moderately evolved with respect to those emitted in 2010, just before the 2010-2014 quiescence. Bulk rock and melt inclusion data suggest that the 2014 evolved magma can be produced by crystal fractionation during the long lasting (4.6 years) storage and cooling of the

890 magma injected and partly erupted in November 2009. The different types of scoria and
891 pumice emitted in 2014 show significant variations in glass composition (Fig. 8b) due to
892 variable degrees of micro-crystallization. In theory, microcrysts can reflect late stage (during
893 magma ascent and post-fragmentation) crystallization. In this case, their variable amount
894 within, for instance, the glassy and opaque parts of the spiny scoria might reflect slower
895 ascent velocity or longer residence time in the system (e.g. Hammer et al., 1999, Stovall et al.,
896 2012; Gurioli et al., 2014) in agreement also with the vesicle signature. However, the four
897 typologies of clasts differ also in terms of mesocryst content (from rare to 5 vol% for the
898 golden and fluidal and 14-23 vol% for the glassy spiny and spiny opaque, respectively).
899 Equilibrium plagioclase-melt pairs record an almost constant and moderate dissolved water
900 content, intermediate between that expected for melts sitting in the main shallow reservoir
901 (located close to sea level) and the degassed matrix of lavas. Dissolved water contents are
902 thus consistent with pre-eruptive magma water degassing during its storage at shallow level,
903 as suggested by geophysical data, and suggest that the plagioclase mesocrysts and some of the
904 microlites in the spiny scoria and in the lava grew during magma storage. Melt composition
905 records a potential pre-eruptive thermal gradient of ~30 °C between the hotter (pumice and
906 fluidal) and the cooler (spiny) magma.

907 Tait et al. (1989) suggest that magma evolution can lead to oversaturation of volatile
908 species within a shallow reservoir and trigger a volcanic eruption. At PdF, the golden and the
909 fluidal clasts might represent the portion of magma located at the top of the shallow reservoir
910 and enriched in bubbles of water rich fluids, released by the cooler, more crystallized and
911 more degassed "spiny-lava" magma (Fig. 10b). The small volume of magma, its constant bulk
912 composition and the very small inflation recorded prior to the eruption (Fig. 1d) could be
913 consistent with an internal source of over-pressure related to volatile exsolution. Larger
914 inflation rates over a broader area are expected when shallow reservoir pressurization is
915 related to a new magma input from a deeper source. Slight baseline extensions both on distal
916 and proximal sites suggest that magma transfer towards shallower crustal levels started short
917 before (11 days) the final magma eruption. Geochemical data do not support the occurrence of
918 a new magma input in the degassed and cooled 2014 reservoir. We can thus speculate that
919 stress field change related to progressive deep magma transfer has promoted volatile
920 exsolution, melt-crystal separation and melt expansion in the shallow reservoir. Textural
921 heterogeneity of the 2014 products partly reflects a pre-eruptive physical gradient recorded by
922 the variability in crystal and bubble contents in the shallow reservoir feeding this eruption.
923 The golden and fluidal fragments are the bubble richer and hotter portion of the melt. The

924 spiny fragments are the degassed and cooler portion of the reservoir, whose progressive

925 tapping led to a decrease in explosive intensity (from fountaining to Strombolian activity).

926 Our results are also consistent with processes of mechanical reservoirs/dyke stratification, as

927 observed by Menand and Phillips (2007). As explained earlier, magma ascent promoted

928 syneruptive degassing induced crystallization. The spiny opaque clasts can be considered as

929 being recycled material that fell back into the system. Accumulation of olivine crystals out of

930 equilibrium with the host magma produces minor variations in mesocryst contents as

931 observed within the same type of clasts sampled at different times/locations during the

932 eruption, with the scoria from the WF and early erupted lava being the ones with the lowest

933 amount of olivine (Table S4 and Fig. 7b). Again, this temporal variation supports an increase

934 in large heavy crystals within the most degassed magma emitted toward the end of activity,

935 further suggesting that it corresponds to the lower part of the reservoir.

936 Our dataset permits us to propose that the 2014 eruption was fed by a physically zoned

937 magma reservoir. The lighter crystal-poor, bubble-rich magma located at reservoir top

938 ascended first, rapidly and fed the early more energetic phase, the Hawaiian fountaining. This

939 lighter magma is not more evolved than the spiny one (same bulk compositions) and it is not

940 necessarily richer in dissolved volatile amounts; it is just poorer in crystal and richer in

941 bubbles. Second boiling, possibly triggered a few days before the eruption by stress field

942 change, is responsible of the extraction of bubble rich melt from a crystal-rich network. This

943 last one is represented by the main volume of the erupted lava. Fast ascent of the foam hinders

944 its crystallization and preserves high number of vesicles, high vesicularity and it is only little

945 modified by post-fragmentation expansion. Decrease in initial overpressure translates in a

946 progressive decrease in magma ascent rate and output rate (e.g. Coppola et al., 2017 and

947 references therein). Nucleation of microcrysts is enhanced in melt ascending with lower speed

948 and is mostly related to syneruptive degassing (for the spiny).

949 The larger volume (dense lava) corresponds to crystallized and less vesiculated magma

950 which experiences a slow ascent in the dyke and even further micro-crystallisation during its

951 subaerial emplacement.

952 Melt inclusion results allow us to confirm the involvement of a single and only slightly

953 heterogeneous magma source in 2014, related to cooling and fractional crystallisation of an

954 older magma batch (November 2009). Interestingly, this latter short lived summit eruption

955 was also characterized by the same large range of pyroclastic products found in 2014 in spite

956 of its more mafic composition.

957   This suggests that bubble accumulation and source pressurisation is highly dependent

958   on the shallow storage depth, which facilitates rapid water exsolution (Di Muro et al., 2016),

959   and it is not necessarily the outcome of slow magma cooling and differentiation (Tait et al.,

960   1989).

961

962   **6. Proposed model for the 2014 eruption and conclusions**

963

964   In this paper we show that textural and petro-chemical study of the eruptive products can be

965   used to characterize the on-going activity at PdF and to constrain both the trigger and the

966   evolution of short-lived and small-volume eruptions. This approach is extremely valuable in i)

967   understanding processes that lead to an eruption which was preceded by short-lived and

968   elusive precursors, and ii) in reconstructing the time evolution of eruptive dynamics in an

969   eruption with poor direct observations.

970   Following the sketch in Figure 12, we infer that residual magma from the 2009

971   eruption ponding at shallow levels experienced long-lasting cooling and crystallization (Fig.

972   12a). Between 2010 and 2014 the volcano progressively deflated (Fig. 12b) possibly because

973   of magma degassing and cooling, facilitated by the shallow depth of the reservoir. During this

974   phase mesocrysts and some microlites formed (Figs. 4e and 10a).

975   The occurrence of deep (>10 km bsl) lateral magma transfer since March-April 2014

976   has been inferred by Boudoire et al., (2017) on the basis of deep (mantle level) seismic

977   swarms and increase in soil CO_2 emissions on the distal western volcano flank. The incipit of

978   magma transfer towards shallower crustal levels is potentially recorded by subtle volcano

979   inflation about 11 days before the June 2014 eruptions (Figs. 1d and 12c). We suspect that

980   these deep processes can have progressively modified the shallow crustal stress field and

981   favoured magma vesiculation and melt-crystal separation. Second boiling could thus have

982   over-pressured the shallow seated reservoir and triggered magma ascent (Fig. 12c).

983   Without this deep magma transfers we believe that the small reservoir activated in

984   2014 would have cooled down completely to form an intrusion (as suggested by the pervasive

985   crystallization of the lava, one of the densest emitted from 2014 to 2017). The 2014 event

986   represented instead the first of a long series of eruptions, whose magmas became

987   progressively less evolved in time (Coppola et al., 2017). In this scenario the trigger

988   mechanisms of 2014 activity are both internal and external in the sense that the small shallow

989   reservoir hosting cooled magma permitted to create the conditions favourable to a second

990   boiling (Fig. 12c, and Tait et al., 1989). The second boiling was likely trigger by an almost

991 undetectable stress field change, and was favoured by the shallow storage pressure of the
992 magma (Fig. 12c) that promotes fast water exsolution and rapid magma response to external
993 triggers. The second boiling possibly contributed to the inflation registered 11 days before the
994 eruption at 1.4-1.7 km (Fig. 12c) caused both by magma expansion and transfer of hot fluids
995 to the hydrothermal system (Lénat et al., 2011).

996   Our data permit to exclude (i) new magma input and/or fluid inputs (CO_2-rich fluids)
997 from deep magmatic levels to trigger the June 2014 eruption. We also exclude (ii) heating and
998 enhanced convection of the shallow magma reservoir (due to heat diffusion without fluid or
999 mass transfer), because this process is very slow. Furthermore, the 2014 minerals do not
1000 record evidences of magma heating. We can exclude equally (iii) deformation of the volcanic
1001 edifice and decompression of the magma reservoir and/or hydrothermal system due to flank
1002 sliding because geodetic data show no evidence of flank sliding able to produce stress change
1003 in the hydrothermal and magmatic system. Geophysical and geochemical data have permitted
1004 to track vertical magma and fluid transfer below the volcano summit in April 2015, that is
1005 about one year after the early deep lateral magma transfer (Peltier et al., 2016). Deep
1006 processes are difficult to detect for any monitoring network.

1007   We conclude that the overpressure, caused by the second boiling, triggered the
1008 eruption. The occurrence of a hydrous almost pure melt at shallow depth permitted its fast
1009 vesiculation upon ascent towards the surface. In turn, fast ascent of the foam (Fig. 12d)
1010 hindered its crystallization and preserved high number of vesicles. Decrease in initial
1011 overpressure translated in a progressive decrease in magma ascent rate and output rate (e.g.
1012 Coppola et al., 2017 and references therein) and a temporal transition from Hawaiian activity
1013 to Strombolian activity (Fig. 12 d). Nucleation of microcrysts was enhanced in melt ascending
1014 with lower speed and in turn this syn-eruptive crystallization favoured bubble
1015 connectivity/permeability in the ascending magma, even for magma at low vesicularity. The
1016 largest volume (dense lava) corresponds to highly-crystallized and degassed magma already
1017 in the reservoir, that experienced a slower ascent in the dyke and even further micro-
1018 crystallisation during its subaerial emplacement.

1019   The texture of the products allowed us to follow the dynamic evolution of the system
1020 in space, from smooth fluidal scoria emitted from rapid jet of lava at the fractures, to a more
1021 stable activity at the MV, and in time. At the MV, in fact, we observed the transition from the
1022 golden and fluidal fragments emitted from Hawaiian fountaining, at the peak of the intensity
1023 of the eruption, to the spiny fragments, emitted from a declining Strombolian activity at the
1024 end of the eruption.

1025   Therefore we here show for the first time that short lived and weak Hawaiian

1026 fountaining and Strombolian events can preserve pyroclast textures that can be considered a

1027 valid approximation to magma ascent and fragmentation conditions before the explosions and

1028 correlate to the eruptive dynamics as well.

1029   To conclude, these results highlight the importance of petrological monitoring, which

1030 can provide complementary information regarding the ongoing volcanic activity to other

1031 geophysical and geochemical monitoring tools commonly used on volcanoes.

1032 **Acknowledgements**

1033 OVPF team and T. Lecocq for monitoring and fieldwork. F. van Wyk de Vries provided an

1034 English revision for the proof. We thank the STRAP project funded by the Agence Nationale

1035 de la Recherche (ANR-14-CE03-0004-04). This research was financed by the French

1036 Government Laboratory of Excellence initiative no. ANR-10-LABX-0006, the Région

1037 Auvergne, and the European Regional Development Fund. This is Laboratory of Excellence

1038 Clervolc contribution number XXXX

1039

1040 **References list**

1041 Albarède, F., and V. Tamagnan (1988), Modelling the recent geochemical evolution of the

1042 Piton de la Fournaise volcano, Réunion island, 1931-1986, *J. Petrol., 29*, 997-1030.

1043 Albarède, F., B. Luais, G. Fitton, M.P. Semet, E. Kaminski, B.G.J Upton, P. Bachèlery, and

1044 J.L. Cheminée (1997), The geo-chemical regimes of Piton de la Fournaise Volcano Réunion.

1045 during the last 530,000 years, *J. Petrol., 38*, 171–201.

1046 Andronico, D., M.D. Lo Castro, M. Sciotto, and L. Spina (2013a), The 2010 ash emissions at

1047 the summit craters of Mt Etna: relationship with seismo-acoustic signals, *J. Geophys. Res.,*

1048 *118*, 51–70, doi:10.1029/2012JB009895.

1049 Andronico, D., J. Taddeucci, A. Cristaldi, L. Miraglia, P. Scarlato, and M. Gaeta (2013b), The

1050 15 March 2007 paroxysm of Stromboli: video-image analysis, and textural and compositional

1051 features of the erupted deposit, Bull. Volcanol., 75, 733, doi:10.1007/s00445-013-0733-2.

1052 Andronico, D., S. Scollo, M.D. Lo Castro, A. Cristaldi, L. Lodato, and J. Taddeucci (2014),

1053 Eruption dynamics and tephra dispersal from the 24 November 2006 paroxysm at South-East

Crater, Mt Etna, Italy, *J. Volcanol. Geotherm. Res., 274*, 78–91, doi:10.1016/j.jvolgeores.2014.01.009.

Bachèlery, P., J.F. Lénat, A. Di Muro, and L. Michon (2016), Active Volcanoes of the Southwest Indian Ocean: Piton de la Fournaise and Karthala. Active Volcanoes of the World. Springer-Verlag, Berlin and Heidelberg, 1-428, DOI 10.1007/978-3-642-31395-0_12.

Boivin, P., and P. Bachèlery (2009), Petrology of 1977 to 1998 eruptions of Piton de la Fournaise, La Réunion Island, *J. Volcanol. Geotherm. Res., 184*, 109–125.

Bombrun, M., A. Harris, L. Gurioli, J. Battaglia and V. Barra (2015), Anatomy of a strombolian eruption: inferences from particle data recorded with thermal video, *J. Geophys. Res., 120*(4):2367-2387. DOI.10.1002/2014BO11556.

Boudoire, G., M. Liuzzo, A. Di Muro, V. Ferrazzini, L. Michon, F. Grassa, A. Derrien, N. Villeneuve, A. Bourdeu, C. Brunet, G. Giudice, and S. Gurrieri (2017), Investigating the deepest part of a volcano plumbing system: evidence for an active magma path below the western flank of Piton de la Fournaise (La Réunion Island), *J. Volcanol. Geotherm. Res*., doi: 10.1016/j.jvolgeores.2017.05.026.

Brenguier, F., P. Kowalski, T. Staudacher, V. Ferrazzini, F. Lauret, P. Boissier, A. Lemarchand, C. Pequegnat, O. Meric, C. Pardo, A. Peltier, S. Tait, N.M. Shapiro, M. Campillo, and A. Di Muro (2012), First Results from the UnderVolc High Resolution Seismic and GPS network deployed on Piton de la Fournaise Volcano, *Seismo. Res. Lett. 83*(7), doi:10.1785/gssrl.83.1.97.

Brugier, Y.A. (2016), Magmatologie du Piton de la Fournaise (Ile de la Réunion): approche volcanologique, pétrologique et expérimentale. Sciences de la Terre. Université d'Orléans, NNT: 2016ORLE2007, pp. 251.

Bureau, H., F. Pineau, N. Métrich, P.M. Semet, and M. Javoy (1998a), A melt and fluid inclusion study of the gas phase at Piton de la Fournaise volcano (Reunion Island), *Chem. Geol. 147*, 115–130.

Bureau, H., N. Métrich, F. Pineau, and M.P. Semet (1998b), Magma-conduit interaction at Piton de la Fournaise volcano (Réunion Island): a melt and fluid inclusion study, *J. Volcanol. Geotherm. Res. 84*, 39–60.

Carey, R.J., M. Manga, W. Degruyter, D. Swanson, B. Houghton, T. Orr, and M. Patrick (2012), Externally triggered renewed bubble nucleation in basaltic magma: the 12 October 2008 eruption at Halemaʻumaʻu Overlook vent, Kīlauea, Hawaiʻi, USA, *J. Geophys. Res., 117*, B11202. doi:10.1029/2012JB009496.

Carey, R.J., M. Manga, W. Degruyter, H. Gonnermann, D. Swanson D, B. Houghton, T. Orr, and M. Patrick (2013), Convection in a volcanic conduit recorded by bubbles, *Geology, 41*(4), 395–398.

Cashman, K.V., and M.T. Mangan (1994) Physical aspects of magmatic degassing II: constraints on vesiculation processes from textural studies of eruptive products, In: Carroll MR, Holloway JR (eds) Volatiles in magmas, Reviews in mineralogy. *Miner. Soc. Am.,* Fredricksberg, pp 447–478.

Clocchiatti, R., A. Havette, and P. Nativel (1979), Relations pétrogénétiques entre les basaltes transitionnels et les océanites du Piton de la Fournaise (Ile de La Réunion, océan Indien) à partir e la composition chimique des inclusions vitreuses des olivines et des spinelles, *Bull. Minér., 102*, 511–525.

Colombier, M., L. Gurioli, T.H. Druitt, T. Shea, P. Boivin, D. Miallier, and N. Cluzel (2017a), Textural evolution of magma during the 9.4-ka trachytic explosive eruption at Kilian Volcano, Chaîne des Puys, France, *Bull. Volcanol., 79*(2), 1-24. doi:10.1007/s00445-017-1099-7.

Colombier, M., F.B. Wadsworth, L. Gurioli, B. Scheu, U. Kueppers, A. Di Muro, and D.B. Dingwel (2017b), The evolution of pore connectivity in volcanic rocks, *Earth Planet. Sci. Lett.*, *462*, 99-109. DOI: 10.1016/j.epsl.2017.01.011.

Colò, L., M. Ripepe, D.R. Baker, and M. Polacci (2010), Magma vesiculation and infrasonic activity at Stromboli open conduit volcano, *Earth Planet. Sc. Lett. 292*(3–4):274–280.

Coppola, D., N. Villeneuve, A. Di Muro, V. Ferrazzini, A. Peltier, M. Favalli, P. Bachèlery, L. Gurioli, A. Harris, S. Moune, I. Vlastélic, B. Galle, S. Arellano, and A. Aiuppa (2017), A Shallow system rejuvenation and magma discharge trends at Piton de la Fournaise volcano (La Réunion Island), *Earth Planet. Sci. Lett. 463*, 13-24.

Corsaro, R., and L. Miraglia (2014), The transition from summit to flank activity at Mt. Etna, Sicily (Italy): Inferences from the petrology of products erupted in 2007–2009, *J. Volcanol. Geother. Res., 275*, 51– 60.

1113 Darcy, H. (1856) Les Fontaines Publiques de la Ville de Dijon, Dalmont, Paris.

1114 Di Muro, A., Métrich, N., Vergani, D., Rosi, M., Armienti, P., Fougeroux, T., Deloule, E.,
1115 Arienzo, I., Civetta, L. (2014), The shallow plumbing system of Piton de la Fournaise Volcano
1116 (La Réunion Island, Indian Ocean) revealed by the major 2007 caldera forming eruption, *J.*
1117 *Petrol., 55*, 1287-1315.

1118 Di Muro, A., T. Staudacher, V. Ferrazzini, N. Métrich, P. Besson, C. Garofalo, and B.
1119 Villemant (2015), Shallow magma storage at Piton de la Fournaise volcano after 2007 summit
1120 caldera collapse tracked in Pele's hairs, chap 9 of Carey, R. J., V. Cayol, M. P. Poland, and D.
1121 Weis (eds.), Hawaiian Volcanoes: From Source to Surface, *American Geophysical Union*
1122 *Monograph 208*, pp 189–212, doi:10.1002/9781118872079.ch9.

1123 Di Muro, A., N. Métrich, P.Allard, A. Aiuppa, M. Burton, B. Galle, and T. Staudacher (2016),
1124 Magma degassing at Piton de la Fournaise volcano, Active Volcanoes of the World, series,
1125 Springer, Bachelery, P., Lenat, J.F, Di Muro, A., Michon L., Editors. Pg. 203-222.

1126 DYNVOLC Database (2017) Observatoire de Physique du Globe de Clermont-Ferrand,
1127 Aubière, France. DOI:10.25519/DYNVOLC-Database. Online access:
1128 http://dx.doi.org/10.25519/DYNVOLC-Database

1129 Eychenne, J., B.F. Houghton, D.A. Swanson, R.J. Carey, and L; Swavely (2015), Dynamics of
1130 an open basaltic magma system: the 2008 activity of the Halemaʻumaʻu Overlook vent,
1131 Kīlauea Caldera. *Earth Planet. Sci. Lett., 409*, 49–60.

1132 Famin, V., B. Welsch, S. Okumura, P. Bachèlery, and S. Nakashima (2009), Three
1133 differentiation stages of a single magma at Piton de la Fournaise (Réunion hotspot). *Geoch.*
1134 *Geoph. Geos. 10*, Q01007. doi:10. 1029/2008GC002015.

1135 Fisk, M.R., B.G.J Upton, C.E. Ford, and W.M. White (1988), Geochemical and experimental
1136 study of the genesis of magmas of Reunion island, Indian Ocean, *J. Geophys. Res., 93*, 4933-
1137 4950.

1138 Forchheimer, P. (1901) Wasserbewegung durch Boden, Z. Ver. Dtsch. Ing. 45:1781–1788.

1139 Formenti, Y, and T.H. Druitt (2003), Vesicle connectivity in pyroclasts and implications for
1140 the fluidisation of fountain-collapse pyroclastic flows, Montserrat (West Indies), *Earth Planet.*
1141 *Sci. Lett., 214*, 561–574.

1142 Gardner, J.E., R.M.E. Thomas, C. Jaupart, and S. Tait (1996), Fragmentation of magma
1143 during Plinian volcanic eruptions, *Bull. Volcanol., 58*, 144–162.

1144 Giachetti, T., T.H. Druitt, A. Burgisser, L. Arbaret, and C. Galven (2010), Bubble nucleation
1145 and growth during the 1997 Vulcanian explosions of Soufrière Hills Volcano, Montserrat, *J.*
1146 *Volcanol. Geotherm. Res., 193*(3–4):215–231. doi:10.1016/j.jvolgeores.2010.04.001.

1147 Gonnermann, H.M., and M. Manga (2013) Dynamics of magma ascent in the volcanic
1148 conduit. In: Fagents, S.A., Gregg, T.K.P., Lopes, R.M.C. (Eds.), Modeling Volcanic Processes:
1149 The Physics and Mathematics of Volcanism. Cambridge University Press, Cambridge.

1150 Gurioli, L., A.J.L. Harris, B.F. Houghton, M. Polacci, and M. Ripepe (2008) Textural and
1151 geophysical characterization of explosive basaltic activity at Villarrica volcano, *J. Geophys.*
1152 *Res., 113*, B08206. doi:10.1029/2007JB005328

1153 Gurioli, L., A.J.L. Harris, L. Colo, J. Bernard, M. Favalli, M. Ripepe, and D. Andronico
1154 (2013), Classification, landing distribution and associated flight parameters for a bomb field
1155 emplaced during a single major explosion at Stromboli, Italy, *Geology, 41*, 559-562, DOI
1156 10.1130/G33967.1.

1157 Gurioli, L., L. Colo', A.J. Bollasina, A.J.L. Harris, A. Whittington, and M. Ripepe (2014),
1158 Dynamics of strombolian explosions: inferences from inferences from field and laboratory
1159 studies of erupted bombs from Stromboli volcano, *J. Geophys. Res., 119*(1),
1160 DOI:10.1002/2013JB010355.

1161 Gurioli, L., D. Andronico, P. Bachelery, H. Balcone-Boissard, J. Battaglia, G. Boudon, A.
1162 Burgisser, S.B. M.R. Burton, K. Cashman, S. Cichy, R. Cioni, A. Di Muro, L. Dominguez, C.
1163 D'Oriano, T. Druitt, A.J.L Harris, M. Hort, K. Kelfoun, J.C. Komorowski, U. Kueppers, J.L.
1164 Le Pennec, T. Menand, R. Paris, L. Pioli, M. Pistolesi, M. Polacci, M. Pompilio, M. Ripepe,
1165 O. Roche, E. Rose-Koga, A. Rust, L. Scharff, F. Schiavi, R. Sulpizio, J. Taddeucci, and T.
1166 Thordarson (2015), MeMoVolc consensual document: a review of cross-disciplinary
1167 approaches to characterizing small explosive magmatic eruptions, *Bull. Volcanol., 77*, 49.
1168 DOI: 10.1007/s00445-015-0935-x.

1169 Hammer, J.E., K.V. Cashman, R.P. Hoblitt, and S. Newman (1999) Degassing and microlite
1170 crystallization during pre-climactic events of the 1991 eruption of Mt. Pinatubo, Philippines,
1171 *Bull. Volcanol. 60*, 355–380.

Harris, A.J.L., N. Villeneuve, A. Di Muro, V. Ferrazzini, A. Peltier, D. Coppola, M. Favalli, P. Bachèlery, J.-L. Foger, L. Gurioli, S. Moune, I. Vlastélic, B. Galle, and S. Arellano (2017), Effusive Crises at Piton de la Fournaise 2014-2015: A Review of a Multi-National Response Model, *Applied Volcanology, 6,* 11, DOI 10.1186/s13617-017-0062-9

Helz, R.T., and C.R. Thornber (1987), Geothermometry of Kilauea Iki lava lake, Hawaii, *Bull. Volcanol., 49*, 651–668.

Hibert, C, A. Mangeney, M. Polacci, A. Di Muro, S. Vergniolle, V. Ferrazzini, B. Taisne, M. Burton, T. Dewez, G. Grandjean, A. Dupont, T. Staudacher, F. Brenguier, N.M. Shapiro, P. Kowalski, P. Boissier, P. Catherine, and F. Lauret (2015), Multidisciplinary monitoring of the January 2010 eruption of Piton de la Fournaise volcano, La Réunion island, *J. Geophis. Res., 120*(5), 3026-3047

Higgins M.-D. (2000). Measurement of crystal size distributions, *American Mineralogist*, 85, 1105-1116.

Houghton, B.F., and C.J.N. Wilson (1989), A vesicularity index for pyroclastic deposits, *Bull. Volcanol., 51*, 451–462. doi:10.1007/BF01078811

Houghton, B.F., D.A. Swanson, R.J. Carey, J Rausch., and A.J Sutton (2011), Pigeonholing pyroclasts, insights from the 19 March 2008 explosive eruption of Kīlauea volcano, *Geology,39*, 263–266, doi:10.1130/G31509.1.

Houghton, B.F., D.A. Swanson, J. Rausch, R.J. Carey, Fagents S.A., and T.R. Orr (2013), Pushing the volcanic explosivity index to its limit and beyond: constraints from exceptionally weak explosive eruptions at Kılauea in 2008, *Geology, 41*(6):627–630

Houghton, B.F., J. Taddeucci, D. Andronico, H.M. Gonnermann, M. Pistolesi, M.R. Patrick, T.R. Orr, D.A. Swanson, M.Edmonds, D. Gaudin, R.J. Carey and P. Scarlato (2016), Stronger or longer: Discriminating between Hawaiian and Strombolian eruption styles, *Geology* doi: 10.1130/G37423.1

Inman, D.L. (1952) Measures for describing the size distribution of sediments, *J. Sed. Petrol., 22*, 125–145.

Kahl, M., S.Chakraborty, M. Pompilio, and F. Costa (2015), Constraints on the nature and evolution of the magma plumbing system of Mt. Etna Volcano (1991–2008) from a combined

thermodynamic and kinetic modelling of the compositional record of minerals, *J.Petrol., 56*, 2025–2068, doi:10.1093/petrology/egv063.

Kawabata, E., S.J. Cronin, M.S. Bebbington, M.R.H. Moufti, N. El-Masry, and T. Wang (2015), Identifying multiple eruption phases from a compound tephra blanket: an example of the AD1256 Al-Madinah eruption, Saudi Arabia, *Bull. Volcanol., 77*, 6 DOI 10.1007/s00445-014-0890-y.

Lange, R.A., H.M. Frey, and J. Hector (2009), A thermodynamic model for the plagioclase-liquid hygrometer/thermometer, *Am. Mineral., 94*, 494–506.

Lautze, N., J. Taddeucci, D. Andronico, C. Cannata, L. Tornetta, P. Scarlato, B. Houghton, and D. Lo Castro (2012), SEM-based methods for the analysis of basaltic ash from weak explosive activity at Etna in 2006 and the 2007 eruptive crisis at Stromboli, *Phys. Chem. Earth 45*,46, 113–127, doi:10.1016/j.pce.2011.02.001.

Leduc, L., L. Gurioli, A.J.L. Harris, L. Colo', and E. Rose-Koga (2015), Types and mechanisms of strombolian explosions: characterization of a gas-dominated explosion at Stromboli, *Bull. Volcanol., 77*, 8, DOI: 10.1007/s00445-014-0888-5

Lénat, J.-F., P. Bachèlery, and A. Peltier (2011), The interplay between collapse structures, hydrothermal systems and magma intrusions: the case of the central area of Piton de la Fournaise volcano, *Bull. Volc.* doi:10.1007/s00445-011-0535-3

Lénat, E.F., P.B. Bachelery, and O. Merle (2012), Anatomy of Piton de la Fournaise volcano (La Réunion, Indian Ocean), *Bull. Volcanol. 74*, 1945–1961.

Lengliné, O, Z. Duputel, and V. Ferrazzini (2016), Uncovering the hidden signature of a magmatic recharge at Piton de la Fournaise volcano using small earthquakes, *Geophys. Res. Lett., 43*, doi: 10.1002/2016GL068383

Lindoo, A., J.F. Larsen, K.V. Cashman, A.L. Dunn, and O.K Neill (2016), An experimental study of permeability development as a function of crystal-free melt viscosity, *Earth Planet. Sci. Lett., 435*, 45–54, doi: 10 .1016 /j .epsl .2015 .11 .035.

Lindoo, A., J.F. Larsen, K.V. Cashman, and J. Oppenheimer (2017), Crystal controls on permeability development and degassing in basaltic andesite magma, *Geology, 45*(9), p. 831-834.

Liuzzo, M., Di Muro, A., Giudice, G., Michon, L., Ferrazzini, V., and Gurrieri, S. (2015), New evidence of CO2 degassing anomalies on the Piton de la Fournaise volcano and the link with volcano tectonic structures Geochemistry, Geophysics, Geosystems, 16, doi:10.1002/2015GC006032.

Mangan, M.T., and K.V. Cashman (1996), The structure of basaltic scoria and reticulite and inferences for vesiculation, foam formation, and fragmentation in lava fountains. *J. Volcanol. Geotherm. Res., 73*, 1–18.

Menand, T., and J.C. Phillips (2007), Gas segregation in dykes and sills. *J. Volcanol. Geother. Res.*, *159*(4), 393–408. https://doi.org/10.1016/j.jvolgeores.2006.08.003.

Michon, L., A. Di Muro, N. Villeneuve, C. Saint-Marc, P. Fadda, and F. Manta (2013), Explosive activity of the summit cone of Piton de la Fournaise volcano (La Réunion Island): a historical and geological review, *J. Volcanol. Geotherm. Res. 263*, 117-133.

Moitra, P., H.M. Gonnermann, B.F. Houghton, and T. Giachetti (2013), Relating vesicle shapes in pyroclasts to eruption styles, *Bull. Volcanol*. 75, 691. doi:10.1007/s00445-013-0691-8

Morgan D.J., and D.A. Jerram (2006), On estimating crystal shape for crystal size distribution analysis, *J. Volc. Geotherm. Res., 154*, 1–7.

Moune, S., O. Sigmarsson, P. Schiano, T. Thordarson, and J.K. Keiding (2012), Melt inclusion constraints on the magma source of Eyjafjallajökull 2010 flank eruption, *J. Geophys. Res., 117*, B00C07, doi:10.1029/2011jb008718.

Morandi, A., C. Principe, A. Di Muro, G. Leroi, L. Michon, and P. Bachèlery (2016), Pre-historic explosive activity at Piton de la Fournaise volcano. In: Bachèlery P, Lénat JF, Di Muro A, Michon L (eds) Active Volcanoes of the Southwest Indian Ocean: Piton de la Fournaise and Karthala. Active Volcanoes of the World. Springer-Verlag, Berlin and Heidelberg, pp 107–138

Óladóttir, B., O. Sigmarsson, G. Larsen, and J.-L. Devidal (2011), Provenance of basaltic tephra from Vatnajökull subglacial volcanoes, Iceland, as determined by major- and trace-element analyses, *Holocene, 21*, 1037–1048, doi:10.1177/0959683611400456.

1258 Oppenheimer, J., A.C. Rust, K.V. Cashman, and B. Sandnes (2015), Gas migration regimes
1259 and outgassing in particle-rich suspensions, *Frontiers in Physics, 3*, 1–13, doi: 10 .3389 /fphy
1260 .2015 .00060.

1261 Ort, M.H., A. Di Muro, L. Michon, and P. Bachèlery (2016), Explosive eruptions from the
1262 interaction of magmatic and hydrothermal systems during flank extension: the Bellecombe
1263 Tephra of Piton de La Fournaise (La Réunion Island), *Bull. Volcanol. 78*, 5,
1264 doi:10.1007/s00445-015-0998-8.

1265 Papale P., R. Moretti, and D. Barbato (2006), The compositional dependence of the saturation
1266 surface of $H_2O + CO_2$ fluids in silicate melts, *Chemical Geology*, 229, 1/3, 78-95,
1267 doi:10.1016/j.chemgeo.2006.01.013.

1268 Parcheta, C.E., B.F. Houghton, and D.A. Swanson (2013), Contrasting patterns of vesiculation
1269 in low, intermediate, and high Hawaiian fountains: a case study of the 1969 Mauna Ulu
1270 eruption, *J. Volcanol. Geotherm. Res., 255*, 79–89

1271 Peltier, A., P. Bachèlery, and T. Staudacher (2009), Magma transport and storage at Piton de la
1272 Fournaise (La Réunion) between 1972 and 2007: A review of geophysical and geochemical
1273 data. *J. Volcanol.Geother. Res., 184,* 93-108.

1274 Peltier, A., F. Beauducel, N. Villeneuve, V. Ferrazzini, A. Di Muro, A. Aiuppa, A. Derrien, K.
1275 Jourde, and B. Taisne (2016), Deep fluid transfer evidenced by surface deformation during the
1276 2014–2015 unrest at Piton de la Fournaise volcano, *J. Volcanol. Geotherm. Res., 321*, 140–
1277 148. http://dx.doi.org/10.1016/j.jvolgeores.2016.04.031.

1278 Polacci, M., R. Corsaro, and D. Andronico (2006), Coupled textural and compositional
1279 characterization of basaltic scoria: insights into the transition from Strombolian to fire
1280 fountain activity at Mount Etna, Italy, *Geology, 34*(3), 201–204. doi:10.1130/G223181.1.

1281 Polacci, M., C. Bouvet de Maisonneuve, D. Giordano, M. Piochi, L. Mancini L., W.
1282 Degruyter, and O. Bachmannng (2014), Permeability measurements of Campi Flegrei
1283 pyroclastic products: an example from the Campanian Ignimbrite and Monte Nuovo
1284 eruptions. *J. Volcanol. Geotherm. Res. 272*, 16–22.

1285 Putirka, K.D. (2008), Thermometers and barometers for volcanic systems, *Rev. Mineral.*
1286 *Geochem. 69*, 61-120.

1287 Reynolds, O. (1900) Papers on Mechanical and Physical Subjects, Cambridge University
1288 Press.

1289 Roeder, P., E. Gofton, and C. Thornber (2006), Cotectic proportions of olivine and spinel in
1290 olivine-tholeiitic basalt and evaluation of pre-eruptive processes, *J. Petrol., 47*, 883-900.

1291 Roult, G., A. Peltier, T. Staudacher, V. Ferrazzini, B. Taisne, A. Di Muro, and The OVPF
1292 Team (2012), A comprehensive classification of the Piton de la Fournaise eruptions (La
1293 Réunion Island) spanning the 1986–2010 period. Search for eruption precursors from the
1294 broad-band GEOSCOPE RER station analysis and interpretation in terms of volcanic
1295 processes, *J. Volcanol. Geotherm. Res., 241*, 78–104.

1296 Rust, A.C., and K.V. Cashman (2011), Permeability controls on expansion and size
1297 distributions of pyroclasts, *J. Geophys. Res., 116*, B11202.

1298 Saar, M.O., M. Manga, K.V. Cashman, and S. Fremouw (2001) Numerical models of the
1299 onset of yield strength in crystal-melt suspensions: *Earth Planet. Sci. Lett., 187*, 367–379, doi:
1300 10 .1016 /S0012 -821X (01)00289 -8.

1301 Salaün, A., Villemant, B., Semet, M.P., and T. Staudacher (2010), Cannibalism of olivine-rich
1302 cumulate xenoliths during the 1998 eruption of Piton de la Fournaise (La Réunion hotspot):
1303 Implications for the generation of magma diversity. *J.Volcanol. Geother. Res., 198*, 187-204.

1304 Schiano, P., K. David, I. Vlastélic, A. Gannoun, M. Klein, F. Nauret, and Bonnand P. (2012),
1305 Osmium isotope systematics of historical lavas from Piton de la Fournaise (Réunion Island,
1306 Indian Ocean), *Contrib. Mineral. Petrol.,* http://dx.doi.org/10.1007/s00410-012-0774-0.

1307 Shea, T., (2017) Bubble nucleation in magmas: a dominantly heterogeneous process? *J.*
1308 *Volcanol. Geotherm. Res. 343,* 155–170.

1309 Shea, T., B.F. Houghton, L. Gurioli, K.V. Cashman, J.E. Hammer, and B. Hobden (2010),
1310 Textural studies of vesicles in volcanic rocks: an integrated methodology, *J. Volcanol.*
1311 *Geotherm. Res., 190*, 271–289.

1312 Shea, T., L. Gurioli, and B.F. Houghton (2012), Transitions between fall phases and
1313 pyroclastic density currents during the AD 79 eruption at Vesuvius: building a transient
1314 conduit model from the textural and volatile record, *Bull. Volcanol., 74*, 2363–2381,
1315 doi:10.1007/s00445-012-0668-z.

1316 Sparks, R.S.J. (1978), The dynamics of bubble formation and growth in magmas: a review

1317 and analysis, *J. Volcanol. Geotherm. Res., 3*, 1–37.

1318 Sparks, R.S.J. (2003). Forecasting volcanic eruptions, *Earth Planet. Sci. Lett., 210*, 1–15.

1319 Spina, L., C. Cimarelli, B. Scheu, D. Di Genova, and D. B. Dingwell (2016) On the slow

1320 decompressive response of volatile- and crystal-bearing magmas: An analogue experimental

1321 investigation, *Earth Planet. Sci. Lett., 433*, 44-53.

1322 Staudacher, T., and A. Peltier (2015), Ground deformation at Piton de la Fournaise (La

1323 Réunion Island), a review from 20 years of GNSS monitoring, In: Bachèlery P, Lénat, JF, Di

1324 Muro A, Michon L (ed) Active volcanoes of the Southwest Indian Ocean: Piton de la

1325 Fournaise and Karthala. Active volcanoes of the world. Springer, Berlin, 139-170.

1326 doi:10.1007/978-3-642-31395-0_9

1327 Staudacher, T., V. Ferrazzini, A. Peltier, P. Kowalski, P. Boissier, P. Catherine, F. Lauret, and

1328 F. Massin (2009), The April 2007 eruption and the Dolomieu crater collapse, two major

1329 events at Piton de la Fournaise (La Re¤union Island, Indian Ocean). *J. Volcanol. Geother. Res.

1330 184*, 126-137, doi:10.1016/j.jvolgeores.2008.11.005.

1331 Stovall, W.K., B.F. Houghton, H.M. Gonnermann, S.A. Fagents, and D.A. Swanson (2011),

1332 Eruption dynamics of Hawaiian-style fountains: the case study of episode 1 of the Kīlauea Iki

1333 1959 eruption, *Bull. Volcanol. 73*, 511–529. doi:10.1007/s00445-010-0426-z.

1334 Stovall, W.K., B.F. Houghton, J.E. Hammer, S.A. Fagents, and D.A. Swanson (2012),

1335 Vesiculation of high fountaining Hawaiian eruptions: episodes 15 and 16 of 1959 Kīlauea Iki,

1336 *Bull. Volcanol., 74*, 441–455, doi:10.1007/s00445-011-0531-7.

1337 Swanson, D.A., K. Wooten, and T. Orr (2009), Buckets of ash track tephra flux from

1338 Halema'uma'u crater, Hawai'i. *Eos Trans. AGU, 90*, 427–428. doi:10.1029/2009EO460003.

1339 Taddeucci, J., M. Pompilio, and P. Scarlato (2002), Monitoring the explosive activity of the

1340 July–August 2001 eruption of Mt. Etna (Italy) by ash characterization, *Geophys. Res. Lett.,

1341 29*(8), 1029–1032. doi:10. 1029/2001GL014372.

1342 Tait, S., C. Jaupart, and S. Vergniolle (1989), Pressure, gas content and eruption periodicity of

1343 a shallow, crystallising magma chamber, *Earth Planet. Sci. Lett., 92*, 107-123.

Takeuchi, S., S. Nakashima, and A. Akihiko Tomiya (2008) Permeability measurements of natural and experimental volcanic materials with a simple permeameter: toward an understanding of magmatic degassing processes, *J. Volcanol. Geotherm. Res.*, 177:329–339.

Thornber, C.R., K. Hon, C. Heliker, and D.A. Sherrod (2003), A Compilation of Whole-Rock and Glass Major-Element geochemistry of Kīlauea Volcano, Hawai'i, near-vent eruptive products: January 1983 through September 2001: *U.S.G.S. Open File Report*, *03*-477.

Thordarson, T, S Self, N Óskarsson, and T Hulsebosch (1996), Sulfur, chlorine and fluorine degassing and atmospheric loading by the 1783–1784 AD Laki (Skaftár Fires) eruption in Iceland, *Bull. Volcanol. 58*, 205–225.

Villemant, B., A. Salaün, and T. Staudacher (2009), Evidence for a homogeneous primary magma at Piton de la Fournaise (La Réunion): A geochemical study of matrix glass, melt inclusions and Pélé's hairs of the 1998–2008 eruptive activity, *J. Volcanol. Geotherm. Res., 184*, 79–92.

Vlastélic, I., and A.J. Pietruszka (2016), A review of the recent geochemical evolution of Piton de la Fournaise Volcano (1927–2010). In: Bachèlery, P., Lénat, J.F., Di Muro, A., Michon, L. (Eds.), Active Volcanoes of the Southwest Indian Ocean. In: Active Volcanoes of the World, pp.185–201.

Vlastélic, I., A. Peltier, and T. Staudacher (2007), Short-term (1998-2006) fluctuations of Pb isotopes at Piton de la Fournaise volcano (Réunion Island): origins and constraints on the size and shape of the magma reservoir, *Chem. Geology, 244*, 202-220.

Vlastélic, I., C. Deniel, C. Bosq, P. Telouk, P. Boivin, P. Bachèlery, V. Famin,. and T. Staudacher (2009), Pb isotope geochemistry of Piton de la Fournaise historical lavas, *J. Volcanol. Geother. Res., 184*, 63-78.

Vlastélic, I., T. Staudacher, P. Bachèlery, P. Télouk, D. Neuville., and M. Benbakkar (2011) Lithium isotope fractionation during magma degassing: constraints from silicic differentiates and natural gas condensates from Piton de la Fournaise volcano (Réunion Island), *Chemical Geology, 284*, 26–34.

Vlastélic, I., G. Menard, M. Gannoun, J.-L Piro., T Staudacher, and V. Famin (2013), Magma degassing during the April 2007 collapse of Piton de la Fournaise: the record of semi-volatile trace elements (Li, B, Cu, In, Sn, Cd, Re, Tl, Bi), *J. Volcanol. Geother. Res., 254*, 94-107.

1374 Vlastélic, I., A. Gannoun, A. Di Muro, L. Gurioli, P. Bachèlery, and J.M. Henot (2016), Origin

1375 and fate of sulfide liquids in hotspot volcanism (La Réunion): Pb isotope constraints from

1376 residual Fe–Cu oxides, *Geochim. Cosmochim. Acta, 194*, 179-192.

1377 Welsch, B., F. Faure, P. Bachèlery, and V. Famin (2009), Microcrysts record transient

1378 convection at Piton de la Fournaise volcano (La Réunion Hotspot), *J. Petrol., 50*, 2287-2305.

1379 Welsch, B., V. Famin, A. Baronnet, and P. Bachèlery (2013), Dendritic crystallization: a single

1380 process for all textures of olivine in basalts? *J. Petrol., 54*, 539-574.

1381 White, J.D.L., and B.F. Houghton (2006), Primary volcaniclastic rocks, *Geology, 34*, 677–

1382 680, doi:10.1130/G22346.1.

1383 **Figure captions**

1384

1385
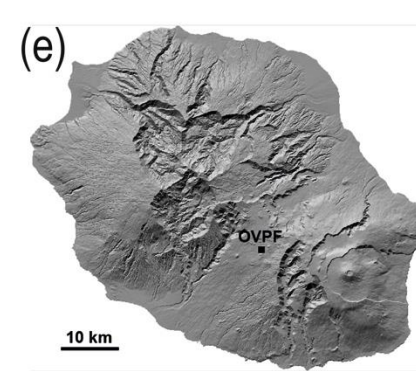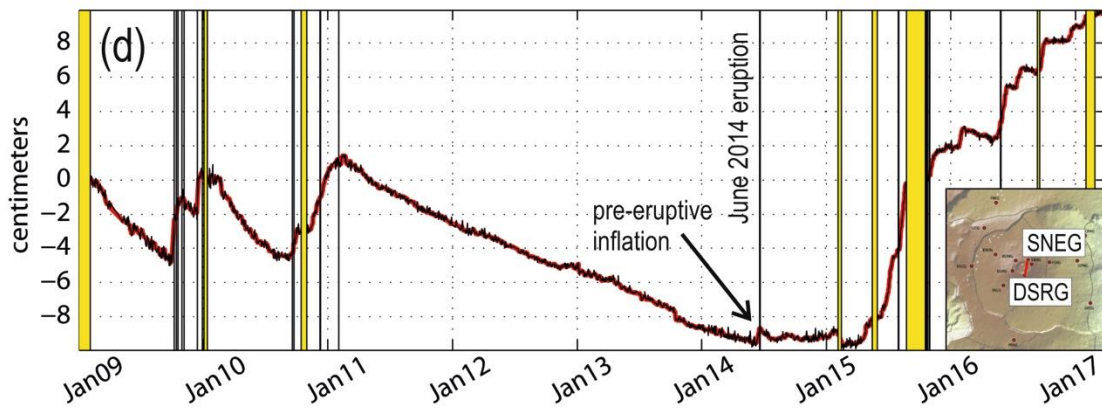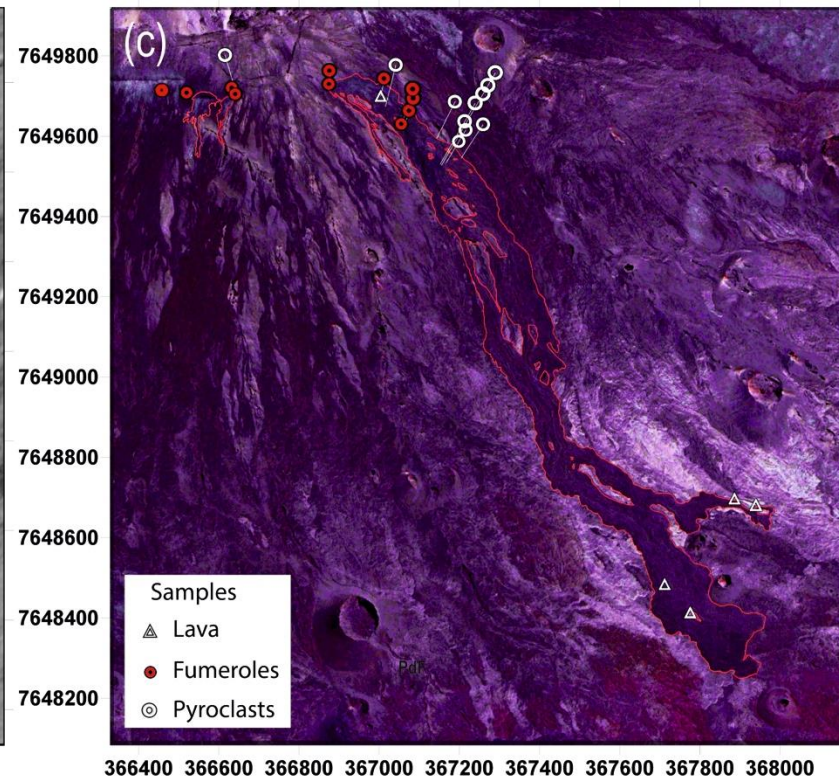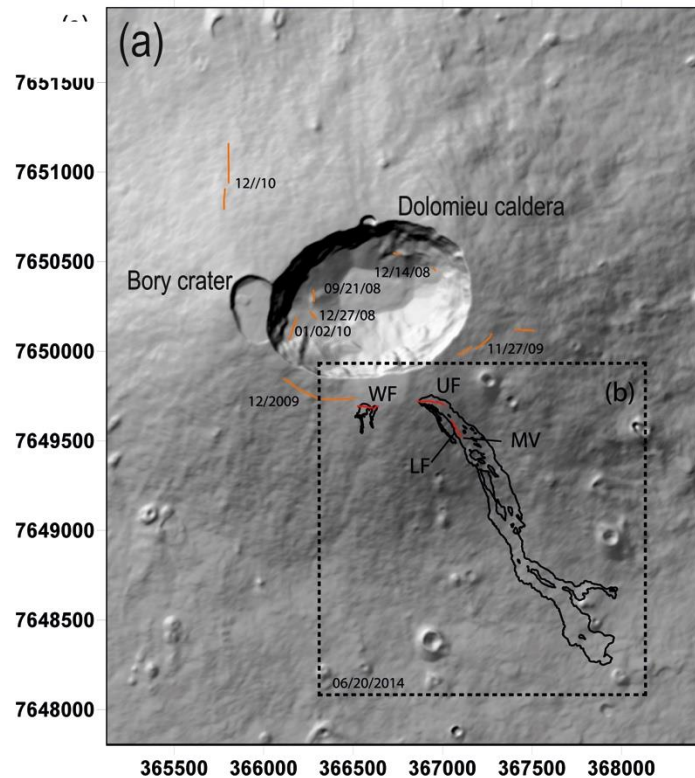
1386   **Figure 1** a) Digital elevation model of the summit crater area at Piton de la Fournaise, La Réunion, France; orange = fractures generated by pre-

1387   2014 eruptions (reported are the dates of their activities); b) red = fractures active during the 2014 eruption: WF (Western Fracture), UF (Upper

1388   Fracture), LF (Lower Fracture), MV (Main Vent). Black= outline of the 2014 lava field; c) locations of sample collection points. The coordinates

1389   are in UTM, zone 40 South. (d) Distance change (baseline) in centimetres between two GNSS summit stations: DSRG and SNEG (see location in

1390   the inset). Increase and decrease of the signal mean a summit inflation and deflation, respectively. The yellow areas represent eruptive and

1391   intrusive periods. In figure 1d, the rapid and strong variations linked to dike injections preceding intrusions and eruptions by a few tens of

1392   minutes have been removed; (e) Digital Elevation Model of La Réunion island.

1393

1394

June 2014 eruption at PdF

Early morning, June 21

June 21 ~ 7h00

June 21, 7h38

June 21, 13h35

June 21,17h00

Figure 2 Photos collection from the 2014 eruption at the MV, highlighted with a white cross (see location in Fig. 1). From a to g: evolution of the Strombolian activity from early morning to evening, June 21 that shows a decline in the activity with time. Unfortunately, the more energetic Hawaiian fountaining events that happened during the night were not documented. a) Strombolian activity at the MV and associated lava flow; b) zoom view of the Strombolian activity at the MV. The images in a, b and the inset in b are from Laurent Perrier; c) aerial view of the SE flank of the PdF, taken by the OVPF team from the helicopter of the gendarmerie of La Réunion; d) Eastern front of the lava where the OVPF team collected a quenched lava sample; e) low Strombolian activity at the MV and the associated lava flow, photo from: http://www.ipreunion.com/volcan/reportage/2014/06/21/eruption-du-piton-de-la-fournaise-actualise-a-17h-la-lave-coule-sur-1-5-kilometre,26023.html; f) and g) decline of the Strombolian activity at the MV, the photo in e) is from   http://www.zinfos974.com/L-eruption-du-Piton-de-la-Fournaise-Le-point-de 17h_a72981.html; and the photo if f) is from: f) http://nancyroc.com/eruption-a-la-reunion

1422
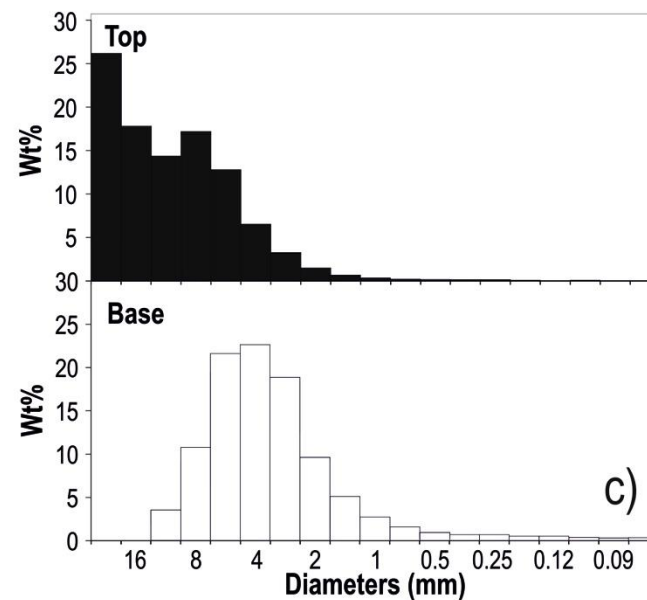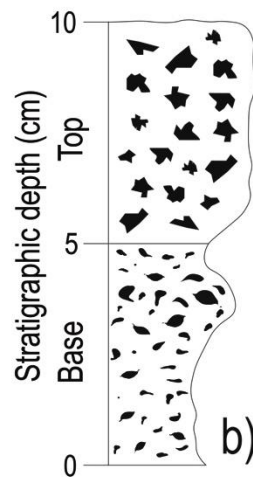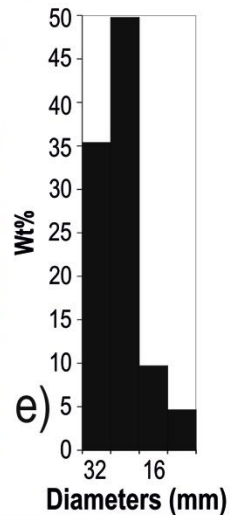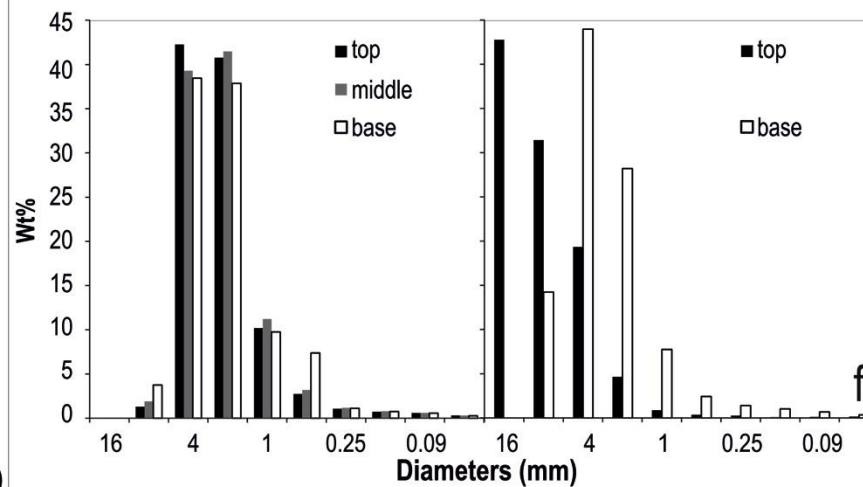
1423   **Figure 3** a) Continuous blanket of scoria fall out deposit emitted from the MV (Fig. 1 for location) during June 2014 eruption at PdF. The black

1424   cross locates the position of the MV (see Fig. 1 for the location); b) schematic stratigraphic log of the scoria fall out deposit emplaced during

1425   June 2014 eruption at the MV. c) grain size histograms of the base and the top of the deposit of the MV, the particle diameters are at half phi; d)

1426   scattered scoria (outlined in yellow) from the WF (see Fig. 1 for the location); e) grain size histogram of the scoria deposit at the WF, the particle

1427   diameters are at half phi; f) comparison between the grain size histograms for the 2010 Hawaiian fountaining and the 2014 MV activity, both the

1428   particle axes are reported in full phi for comparison.

1429

1430

1431

1432

1433
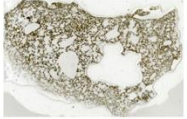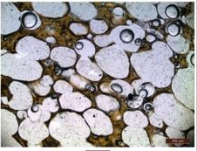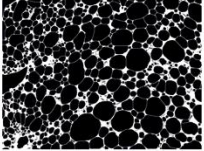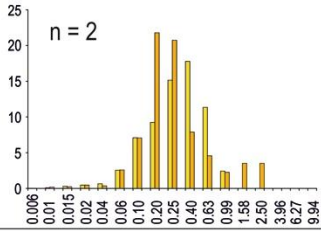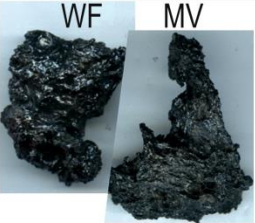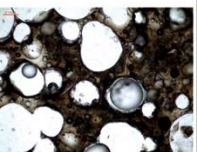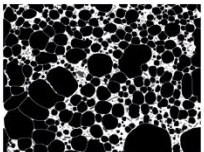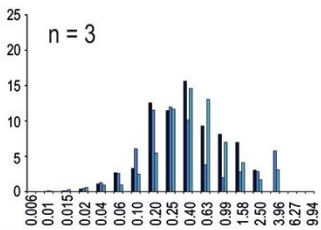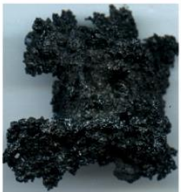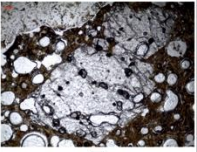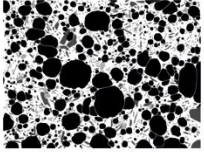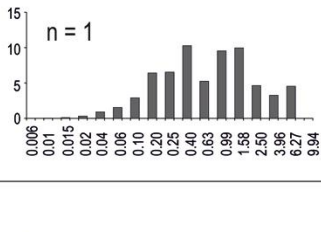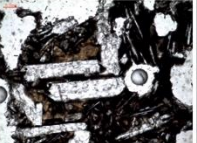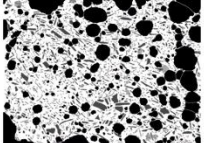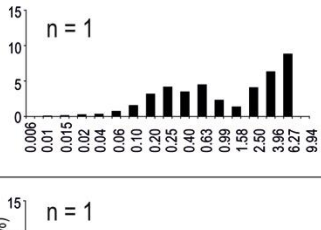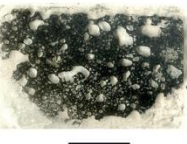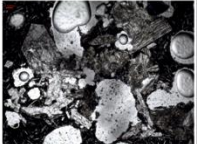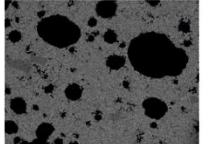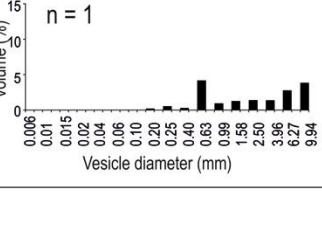
1434

1435

1436

1437

1438

Type	Clast	Thin section	Microscope	SEM (25X)	VSD	Crystal vol %	N_v
Golden Pumice (a)			0.02 mm		n = 2	Tot = 8-15 Mplg= rare µplg = 6-11 Mcpx = rare µcpx =(1-3)	2×10^7 9×10^6
Fluidal Scoria (b)	WF MV		0.02 mm		n = 3	Tot = 4-23 Mplg = 0.4-1 µplg = 2-19 Mcpx = 0-1 µcpx = 1-4	2×10^7 5×10^6 3×10^6
Spiny glassy scoria (c)			0.02 mm		n = 1	Tot = 51 Mplg = 11 µplg = 23 Mcpx =15 µcpx = 2	6×10^6
Spiny opaque scoria (d)					n = 1	Tot = 55 Mplg = 11 µplg = 25 Mcpx = 10 µcpx = 9	4×10^6
Lava (e)	1m	1 cm	0.02 mm	1 mm	n = 1	Tot = 100 Mplg = 2 µplg = 64 Mcpx = 3 µcpx = 31	2×10^4

1439

1440 **Figure 4** Textural features of June 2014 pyroclasts and lava. Clast = photo of the different types of juvenile pyroclasts and lava channel. The

1441 photo of the lava channel is from Laurent Perrier. WF = Western Fracture (smooth fluidal scoria), MV = Main Vent (fluidal scoria, less smooth

1442 than the ones at the WF). Thin section = thin section imaged with a desktop scanner. Microscope = picture taken with an optical microscope

1443 using natural light; SEM (25X) = image captured using a scanning electron microscopy (SEM), in BSE mode at 25x magnification: black are

1444 vesicles, white is glass, grey are crystals. VSD = vesicle volume distribution histograms, where the diameter, in mm, is plotted versus the volume

1445 percentage, n = number of measured clasts; Crystal vol. % : Tot = total percentage of crystals corrected for the vesicularity; Mplg = percentage

1446 of mesocrysts of plagioclase; μplg = percentage of microcrysts of plagioclase; Mcpx = percentage of mesocrysts of pyroxene; μcpx = percentage

1447 of microcrysts of pyroxene; Nv = number density corrected for the vesicularity.

1448

1449

1450
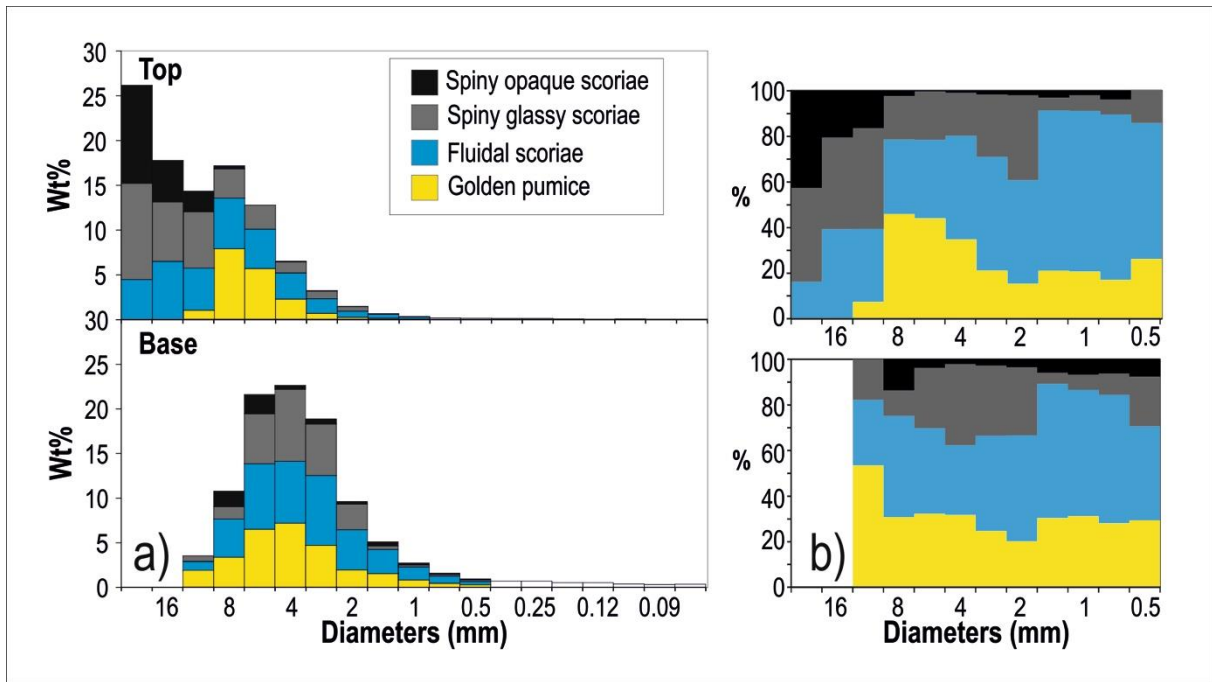
1451

1452 **Figure 5** Proportion of each type of clast measured from the base to the top of the 10 cm thick
1453 deposit emplaced during the eruption, at the MV site. The deposit is dominated by Hawaiian-
1454 like lapilli fragments at the base (golden pumice and fluidal scoria) and Strombolian-like
1455 bombs and lapilli at the top (spiny scoria): (a) componentry within the different grain size
1456 classes; b) normalized componentry composition from the base to the top of the deposit.

1457

1458

1459

1460

1461

1462

1463

1464

1465
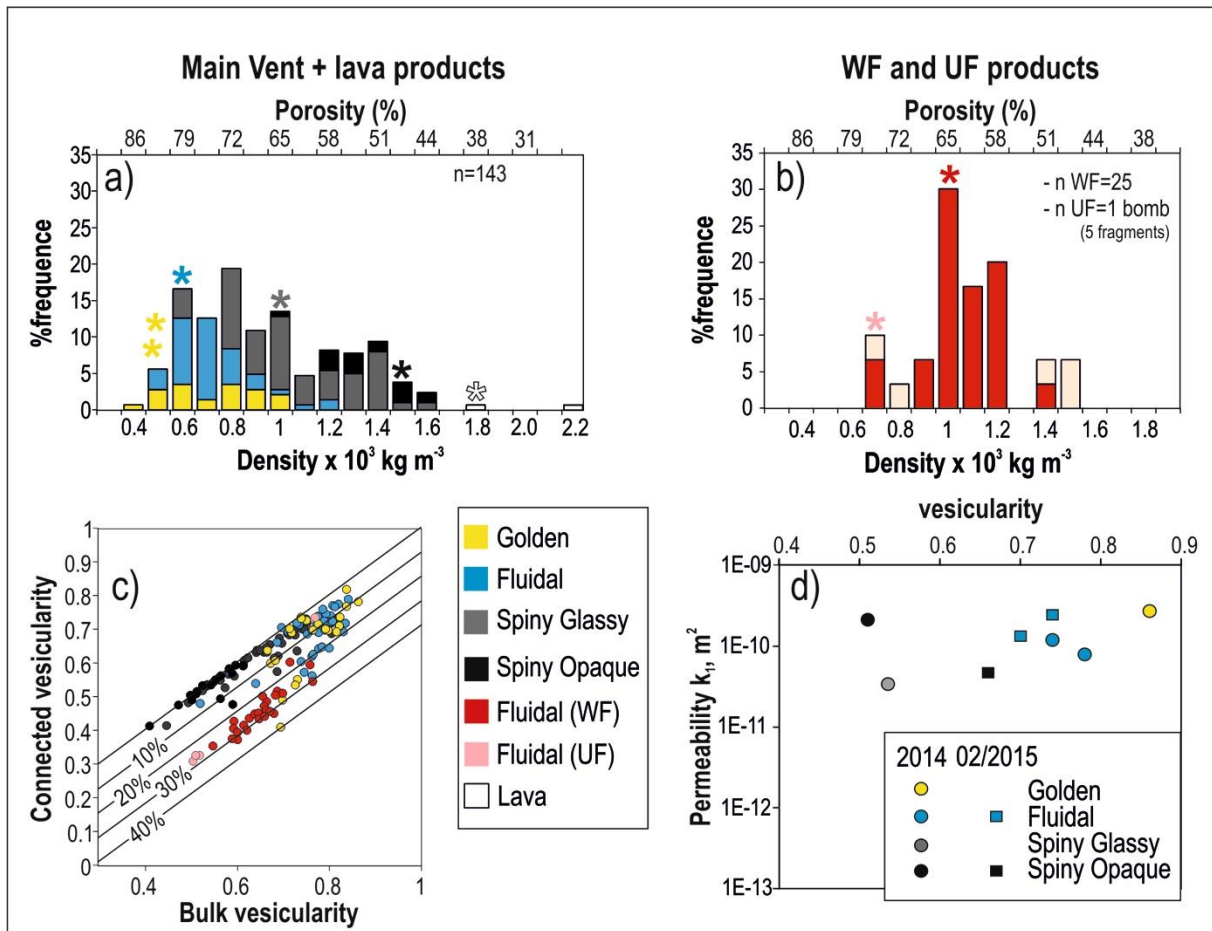
Figure 6 Density, connectivity and permeability data of June 2014 pyroclast and lava fragments: a) density distribution histogram for all the pyroclast fragments measured at the MV + two lava fragments collected from the Eastern front of the lava flow (see Fig. 1 for location). n = number of measured clasts; b) density distribution histogram for the pyroclasts sampled at the WF and the bomb sampled at the UF. The bomb broke in five fragments (2 fragments from the core, the least dense, and three fragments from the quenched edges, the densest); and c) In both the density histograms the stars represent the density intervals from which we picked the clasts for the textural measurements; c) graph of the connected vesicularity versus total vesicularity. The diagonal line represents equality between the connectivity and vesicularity, beneath this line the samples have isolated vesicles and the straight lines represent lines of equal fraction of isolated vesicles. To note that the bomb from the UF has the high vesicular core with less than 5% of isolated vesicles, while the three low vesicular fragments from the core have more than 25% of isolated vesicles (see pink spots); d) Darcian permeability (k_1) versus the vesicularity fraction. Data from June 2014 eruption and February 2015 eruption are reported.
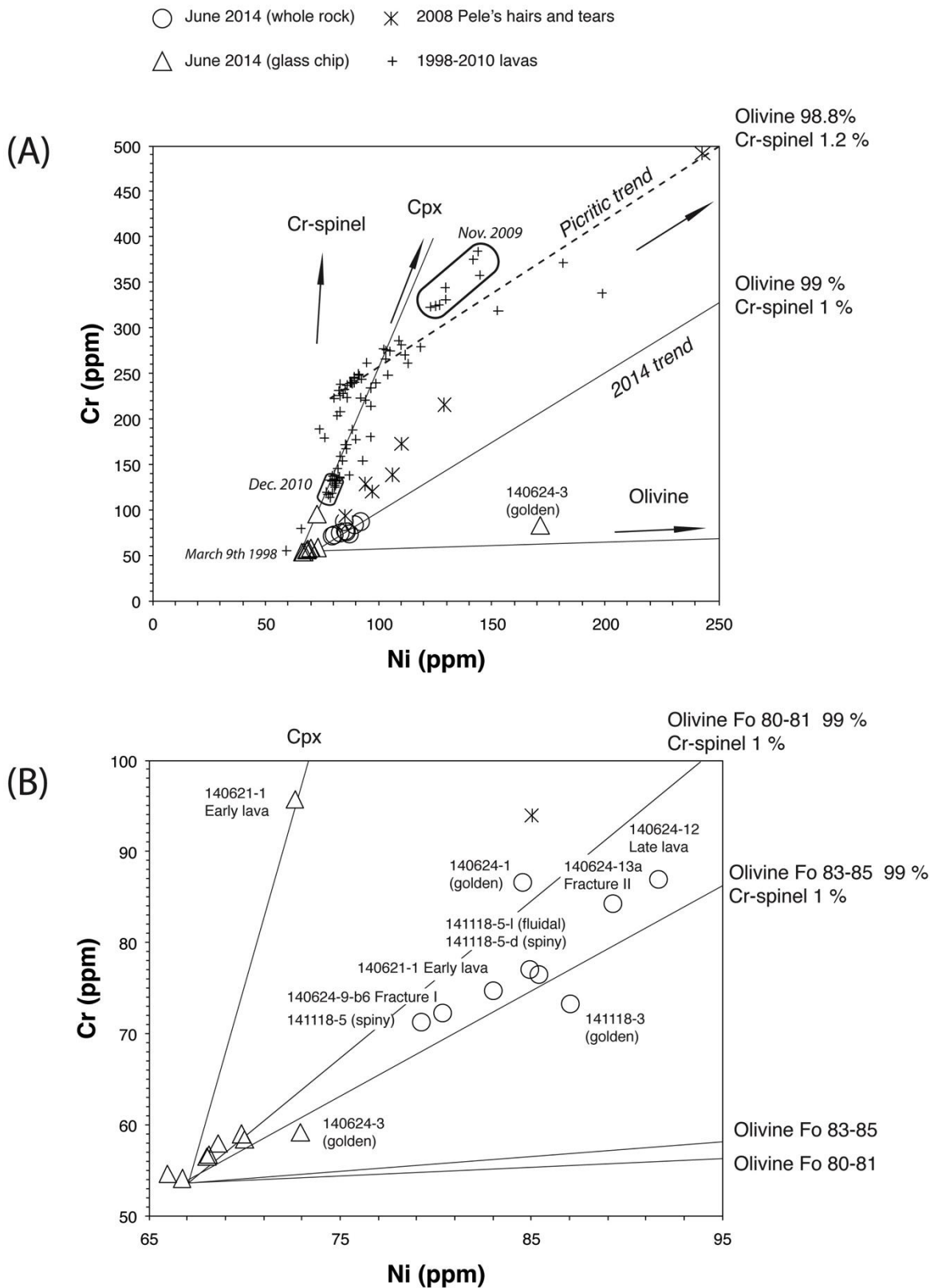
1483

1484 **Figure 7** Ni-Cr concentration plot. (a) Ni-Cr signature of the June 2014 lavas compared to

1485 that of recent eruptions (Di Muro et al. (2015) and unpublished data). Whole-rock (circles)

and glass (triangles) compositions are shown for the June 2014 eruption. Olivine controlled lines are indicated for olivine hosting 1.2 and 0.6 wt.% Cr-spinel. Compositions used for olivine (Ni=1900 ppm, Cr=300ppm), clinopyroxene (Ni=970 ppm, Cr=4800 ppm), and Cr spinel (Ni=1500 ppm, Cr=25%) are inferred from Salaün et al. (2010), Di Muro et al. (2015) and Welsch et al. (2009). (b) Zoom of the Ni-Cr relationship between glass (triangles) and whole-rock (circles) samples from the June 2014 eruption. Fracture I = Western Fracture, Fracture II = Upper Fracture. Careful sample selection has permitted to obtain a set of virtually olivine-cpx free crystals. Any addition of mafic crystals translates into enrichment in Ni-Cr; those samples that contain a few % of crystals (consistent with textural and petrological observation) are slightly enriched in compatible elements.
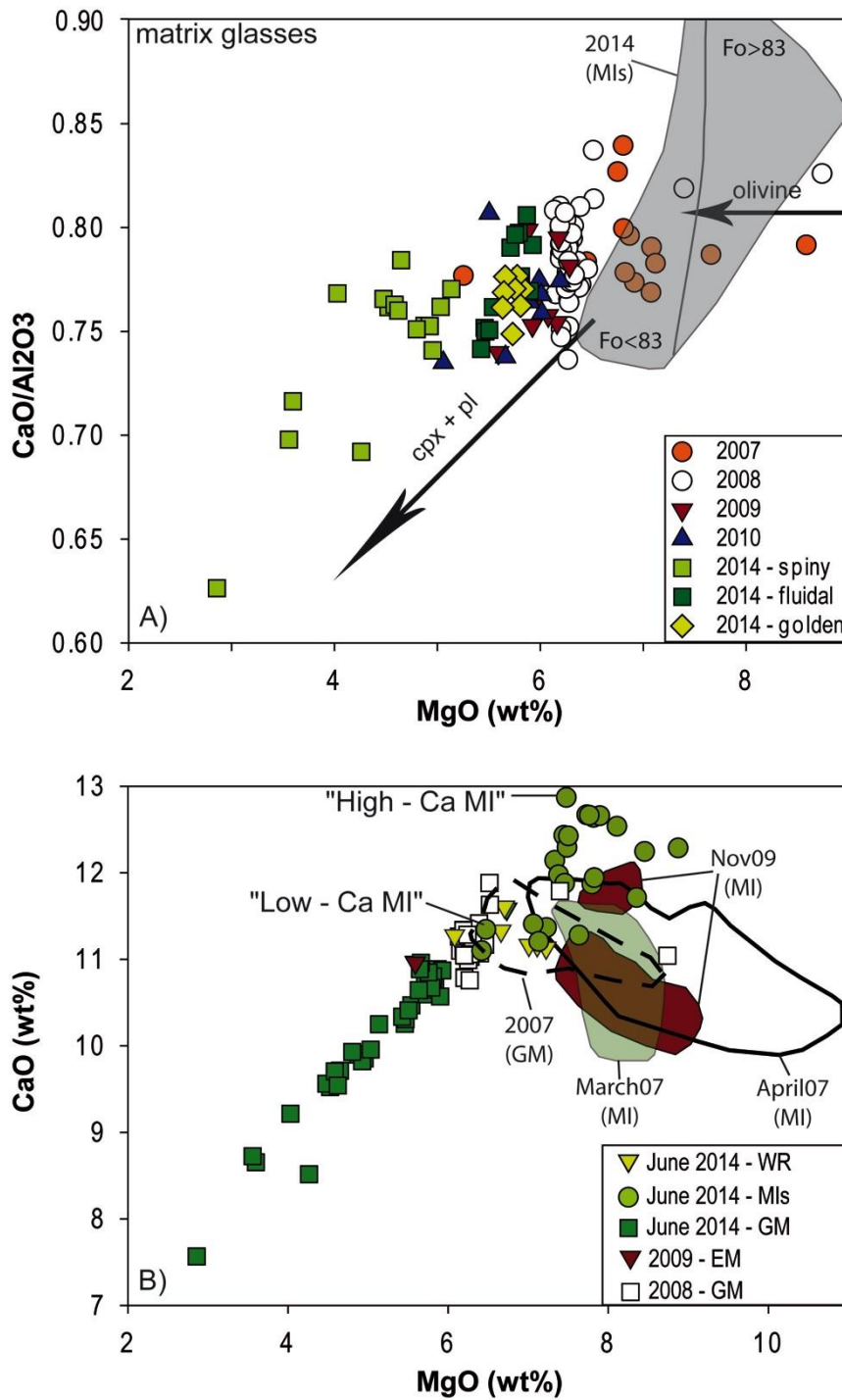
Fig. 8 (a) Evolution of CaO/Al$_2$O$_3$ ratio in the matrix glasses of recent eruptions at Piton de la Fournaise as a function of MgO content (directly proportional to melt temperature). MI = Melt inclusions (grey area for the 2014 samples). (b) CaO versus MgO content for Piton de la Fournaise products. WR = whole rock, GM = ground mass; MI = melt inclusion, EM = embayment glass

1504
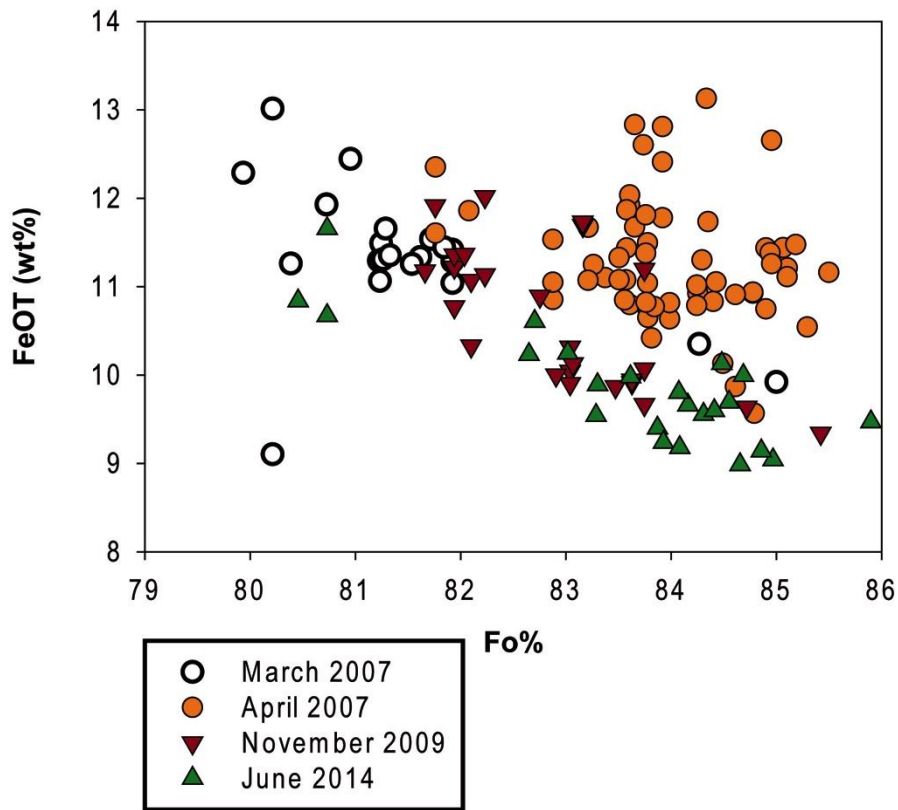
1505

1506 **Figure 9** FeO$_T$ in melt inclusions as function of Fo content of the olivine host for recent
1507 eruptions at Piton de la Fournaise

1508

1509

1510

1511

1512

1513

1514

1515

1516

1517

1518
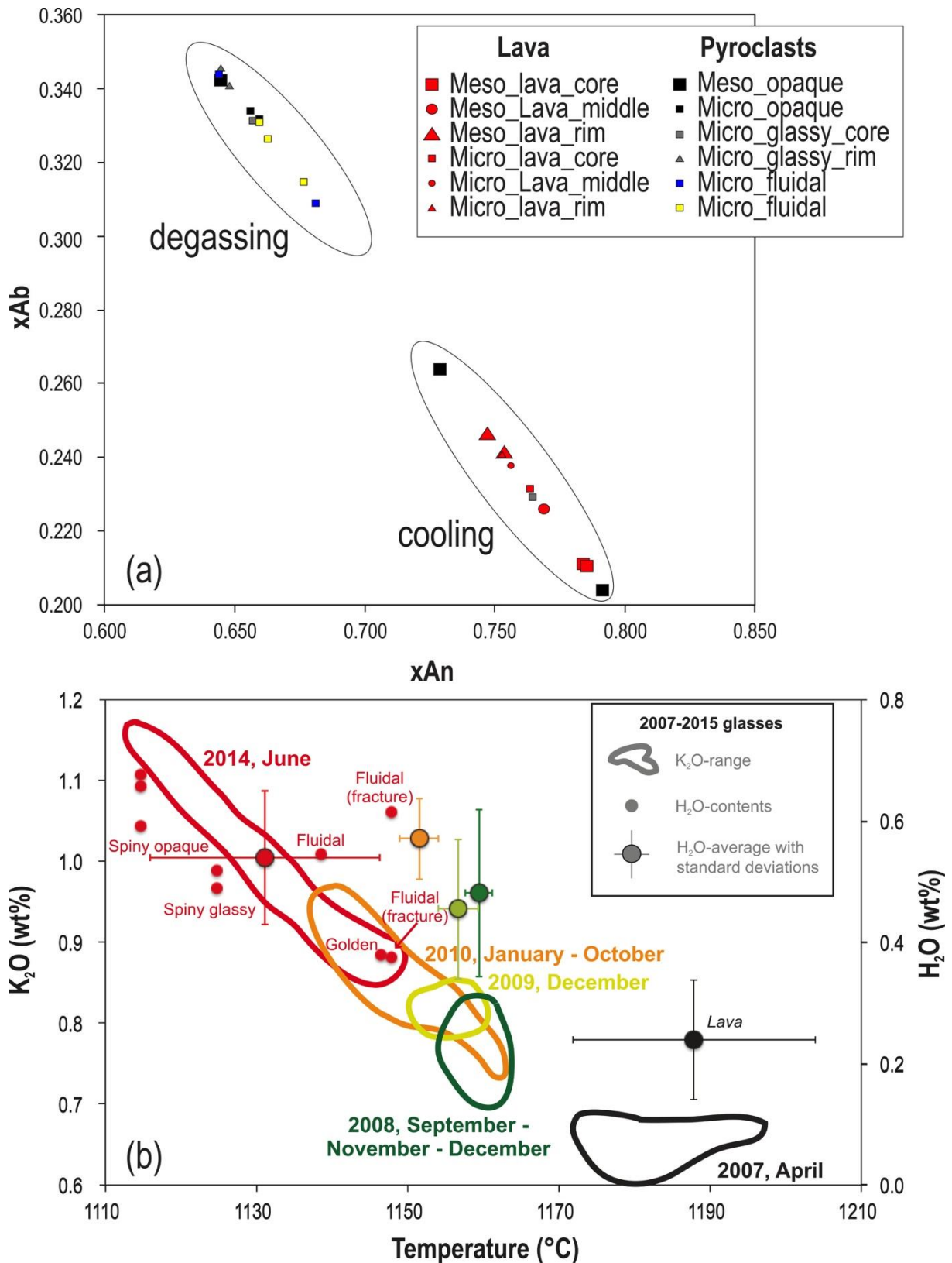
Figure 10 a) Anorthite versus Albite compositions for the plagioclase crystals measured for
June 2014 eruption of PdF; b) Temperature, composition (K_2O) and dissolved water content
(H_2O) for the evolution of 2007-2014 melts from glasses. The data have been obtained by

studying the glass-plagioclase equilibrium or on the basis of matrix glass analyses. Temperature estimation based on the MgO-thermometer of Helz and Thornber (1987) modified by Putirka (2008). Water content from the plagioclase hygrometer of Lange et al. (2009). Only plagioclases in equilibrium with melts are considered, following the procedure described by Putirka (2008) for >1050°C melts (Kd = 0.27±0.05). Error bars reported in Figure 10b correspond to the standard deviation of the plagioclase dataset, whose range is larger than error of the method. We stress that reported temperatures are obtained using Helz dry model; further uncertainty arises from the dependence of the method on dissolved water content as shown recently by Putirka (2008); in order to minimize the number of assumptions and perform a comparison between distinct eruptions, we preferred to adopt the dry model.

1549

1550

1551

1552

1553
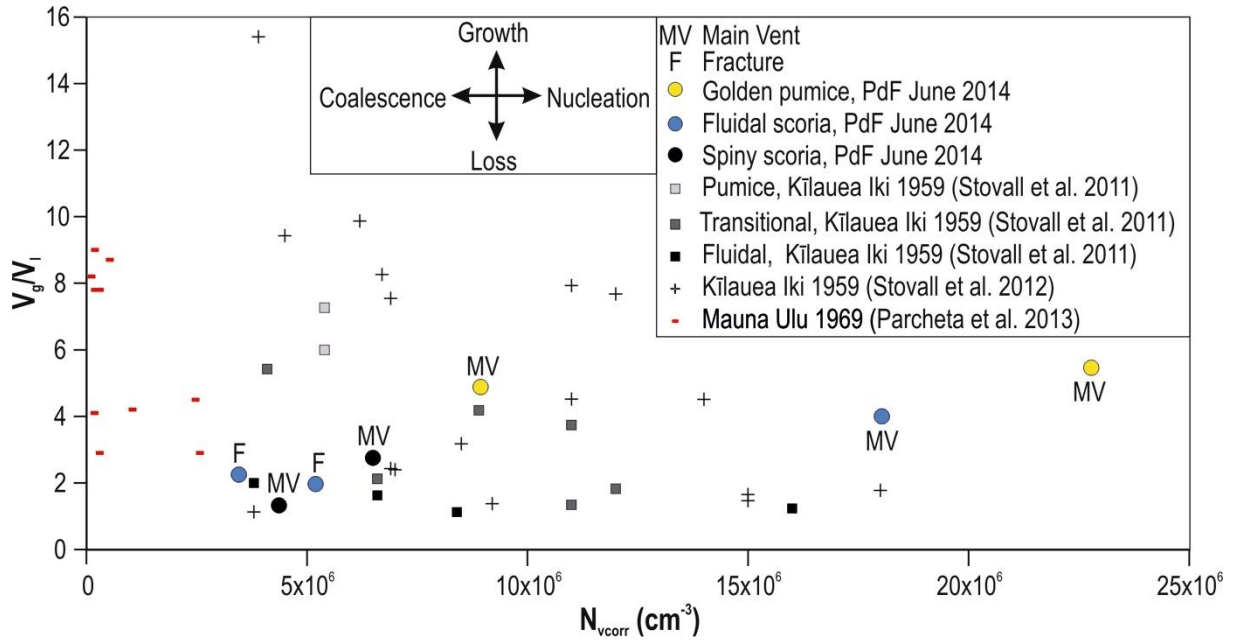
1554

1555 **Figure 11** Volumetric ratio of vesicles to melt (V_G/V_L) versus vesicle number density

1556
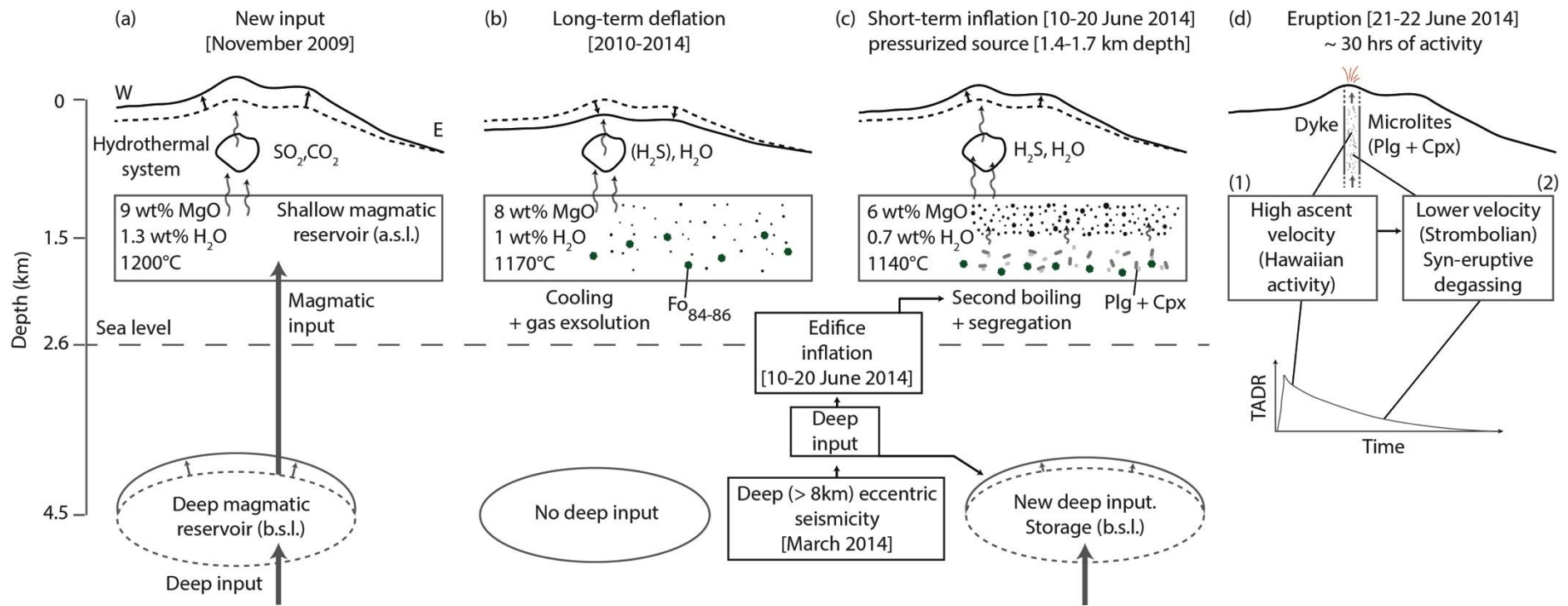
1557

1558 **Figure 12** Schematic model of the evolution of PdF volcanic system from the new deep magmatic input of November 2009 up to June 2014

1559 eruption. See explanation in the text